M.S. THESIS

Study on the Highly Isolated TRx Dual-Polarized Array Antennas for In-Band Full-Duplex Communications

In-Band Full-Duplex 통신용 고격리도 이중편파 송수신기 안테나 어레이에 관한 연구

BY
TAEYEONG YOON

February 2023

DEPARTMENT OF ELECTRICAL AND COMPUTER ENGINEERING
SEOUL NATIONAL UNIVERSITY

Study on the Highly Isolated TRx Dual-Polarized Array Antennas for In-Band Full-Duplex Communications

In-Band Full-Duplex 통신용 고격리도 이중편파 송수신기 안테나 어레이에 관한 연구

지도교수 오 정 석

이 논문을 공학석사 학위논문으로 제출함
2023 년 2 월

서울대학교 대학원
전기·정보 공학부
윤 태 영

윤태영의 공학석사 학위논문을 인준함
2023 년 2 월

위 원 장	남 상 욱	(인)
부위원장	오 정 석	(인)
위 원	유 선 규	(인)

Abstract

In this thesis, we focused on realizing the propagation domain of transmitter and receiver system composed of the antennas and isolators. Firstly, a logical design procedure based on a new perspective of the common mode (CM) and differential mode (DM) theory for a dual-polarized antenna in sub-6 GHz N78 band (3.3-3.8 GHz) has been proposed. Next, novel illumination topologies and decoupling methodologies enabling dual-polarized multi-path coupling suppression for 5G sub-6 GHz transmit/receive (TRx) antenna arrays have been presented.

For the antenna design, a novel elaborate design method using field concentration has been established via the mode segmentation of S-parameters. Interestingly, an improvement in the port isolation between two different polarizations is achieved by using an independently controllable Smith chart trace for each mode using simple methodologies. To provide a deep physical insight into the mechanism of realizing the dual-polarized antenna, the corresponding field distributions based on the CM and DM analysis have been proposed for the first time, and the proposed antenna has been simulated, fabricated, and measured. The simulation as well as experimentally measured results show that the antenna can offer peak isolations of 40 dB, a gain of 8 dBi, cross-polarization discrimination of 20 dB, an efficiency of 92% with stable radiation patterns, and a profile of 0.14λ across 3.3-3.8 GHz, using FR-4 substrates for low-cost. Furthermore, this study not only offers knowledge on cross-polarization but also provides the active S-parameters for all possible amplitude and phase sequences to reflect realistic scenarios.

For the isolator design, the isolator composite consists of the

proposed planar inverted-L isolator (PILI) and electromagnetic band-gap (EBG). To consider dual-polarized multi-path isolations in reliable 5G integration scenarios, a low profile (0.13λ at 3.5 GHz) antenna with dual (±45° slant) polarization, impedance bandwidth of 40%, and port isolation of 25 dB is proposed. It was demonstrated that the proposed PILI could significantly suppress the direct coupling and ground coupling between TRx. Their composite combined with EBGs can further improve their dual-polarized decoupling. Two sets of 3.5GHz 1×4 antenna arrays with 45° - slant polarization and the proposed PILI/EBG composite were designed, manufactured, and measured for simultaneous decoupling of eight paths among the TRx antenna elements. Finally, the measured results reveal that the overall isolation level of the dual-polarized array configuration is approximately 70 dB with a low profile (0.14λ), maintaining the matching and port isolation conditions.

Keyword : Fifth-generation (5G), dual-polarized antenna, low-cost, FR-4, common and differential mode, active s-parameter, XPD, decoupling, isolation, EBG, transmit-receive (TRx) isolation, multi-path isolation, mutual coupling

Student Number : 2021-25750

Contents

List of Tables

List of Figures

Chapter 1. Study Background

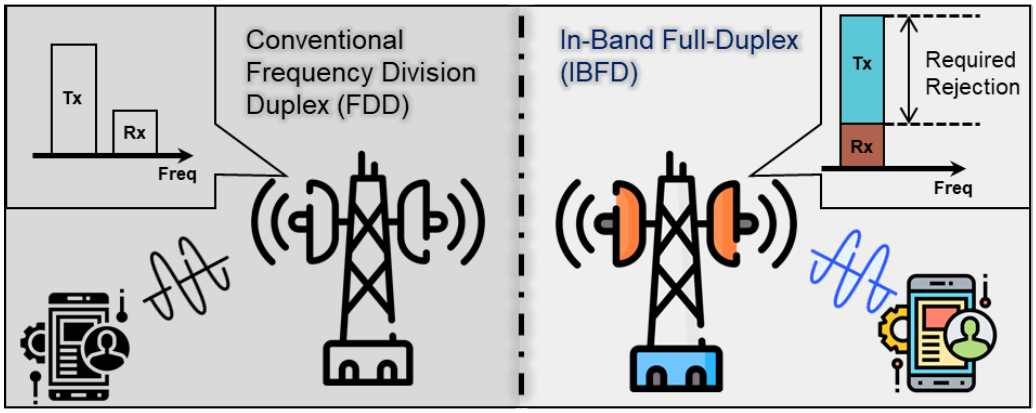

Figure 1. Concept diagrams of FDD and IBFD

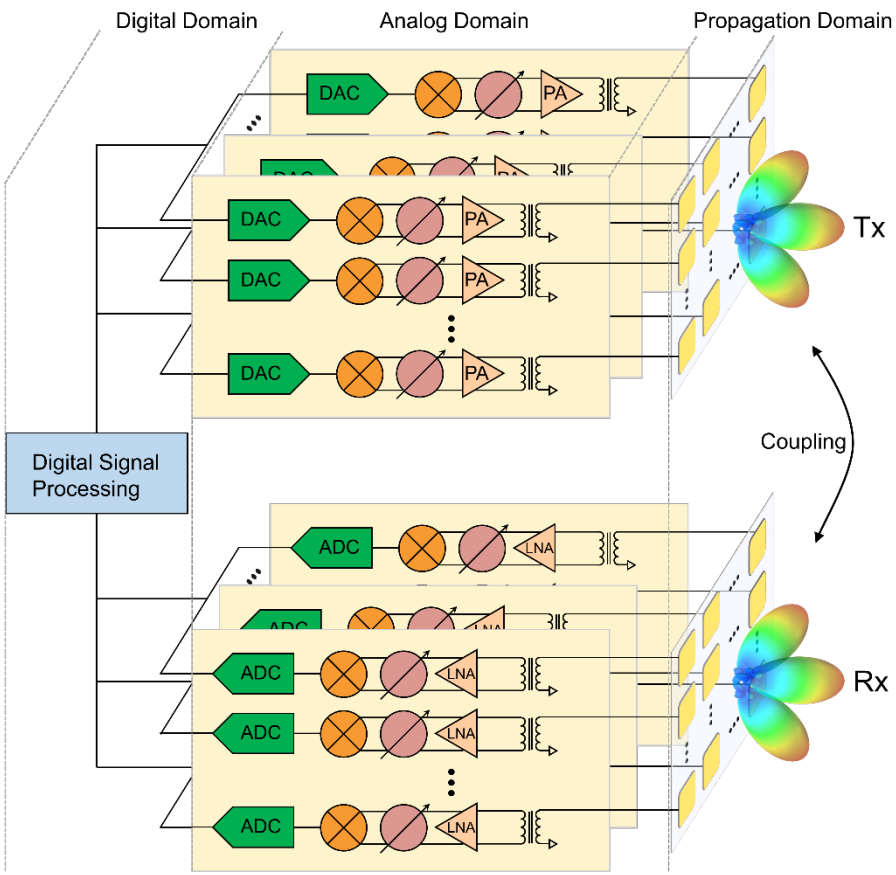

Figure 2. IBFD transceiver, highlighting the propagation, analog, and digital domains.

Recently, antennas with wideband and dual-polarization techniques have become more prevalent in in-band full-duplex (IBFD operation which doubles the spectrum efficiency to fulfill the demands of wireless communication systems owing to their increase capabilities. By using the same frequency band for the transceiver at the same time, IBFD can double spectral efficiency for future wireless networks, such as the fifth-generation (5G) new radio (NR)[1] as depicted in Fig. 1. One of the challenges in adequately implementing an earlier advanced scheme using an array antenna is the requirement of mitigating the mutual coupling between the transmitter and receiver (Tx-Rx).

Meanwhile, self-interference, generated from the mutual coupling between Tx and Rx, refer to itself, which hinders the desired signal from being received by the terminal as shown in Fig. 2. To recognize the effect of self-interference, we have considered the following comprehensive explanations presented in [2]. The proposed data indicates that the self-interference of the base station is greater than 100 dB above the noise floor when the stations and handsets transmit at 21 dBm output power with respect to receiver noise floor. This level is generally obtained using the isolation technology of the propagation, analog, and digital domains. However, in the analog domain, there are many challenges, such as linearity and power efficiency issues. Therefore, to mitigate and reduce design complexity and cost, a scheme that can skip the analog self-interference cancelation by realizing very high isolation in the antenna domain has been presented [3]. Thus, antennas in the Tx-Rx array usually require to maintain a very high isolation level with an appropriate isolator. Using this, self-interference is adequately diminished, leading to improve the performance of the IBFD operation. So this paper focuses on mitigating the isolation for TRx applications. To realize this system, dual-

polarized antennas have been additionally designed with the advanced analysis.

Chapter 2. Antenna Design

2.1 Introduction

Recently, fifth-generation (5G) technology has become a hot topic and has rapidly improved to achieve higher data rates and shorter latency owing to the tremendous amount of signal processing requirement for wireless communication systems [4]. As one of the key methods of 5G systems, dual-polarized antennas are highly desirable for increasing the data throughput in the gradually spaced-limited application scenarios, such as base stations, radars, and satellites. Owing to these advantages and the diverse requirements of various applications, dual-polarized antennas have been widely researched and developed. The N78 band (3.3-3.8 GHz) has been assigned for 5G new radio at sub-6 GHz in many countries. With the advent of the 5G new radio, interest in the 3.5 GHz band has increased quickly and a lot of successful trials have been conducted [5].

To realize the abovementioned technology, different methods have been proposed for its independent operation by mitigating the coupling between two ports of different polarizations. Among the reported approaches for achieving dual-polarized characteristics and adequate bandwidth, differential L-probe feeder with a balun [6], modified feeding line [7], slot coupled [8], suspended parasitic component [9], bowtie dipole [10], magneto-electric dipole [11], and differentially driven patch with open-loop resonator [12] have been the most effectively used methods. In [9], the impedance bandwidth of the two ports was satisfied by the N78 band with $|S_{11}| > 10$ dB by

allocating the parasitic metal stick on the middle of the radiator, while $|S_{21}|$ > 25 dB and cross-polarization discrimination (XPD) > 20 dB were achieved. Using the differential coupling cancellation achieved by a balun, the differentially driven antenna in [6] achieved high port isolation over a wide frequency range, maintaining $|S_{11}|$ > 10 dB, $|S_{21}|$ > 20 dB, and XPD > 20 dB. However, neither of the two studies considered the coupling issue, which is necessary for a realistic environment and conditions between the ports. Therefore, in this study, an active S-parameter analysis, which includes the coupling effect on the matching condition for each port, has been studied for all possible amplitude and phase arrangements.

The common mode (CM) and differential mode (DM) theory presented in this study has been widely used in the design of couplers and power dividers [13]. By utilizing structural symmetry, the complexity of the analysis was reduced, and reliable results were obtained. Recently, methods with these advantages are being actively studied for their application to antenna [14]. In [15], the CM and DM theory was proposed as a method to remove the mutual coupling between two antenna elements. Specifically, methods to improve the isolation performance of dipole and planar inverted-F antennas were introduced and analyzed based on the CM and DM theory. In addition, in [16], decoupling was achieved by using a defected ground structure and the CM and DM analysis between microstrip patch antenna elements, and in [17], isolation was realized by using a connected line between the slot antennas. This was possible because the novel analysis was performed by introducing a new structure while maintaining symmetry. Because these characteristics are maintained even in a dual-polarized antenna, this paper introduces CM and DM analysis of the dual-polarized antenna design to improve the isolation.

Even though the polarization of the ports is different, the dual-polarized antenna's situation has been challenging to achieve a high isolation level so far because the distance between the ports is close and the antennas shared the radiation aperture. Hence, the method of improving the port isolation should be studied.

A simple and useful design method based on a new perspective of CM and DM analysis has been proposed in this study. In our approach, the isolation between two ports having a symmetrical structure is theoretically equivalent to the impedance matching of the CM and DM. Then, the distinctive and apparent field properties of the CM and DM can be used to assist in comprehending the coupling issue and achieving the port isolation by adjusting CM and DM impedances independently. When a similar impedance status for CM and DM is obtained near 50 **Ω**, the coupling current generated by sharing the radiator between the two ports in the passive antenna element can be completely eliminated and the matching condition can be maintained by the superposition of CM and DM. To confirm the feasibility of this method, a practical design example, including the mutual coupling reduction between each port of the dual-polarized antenna, has been proposed. The design example demonstrates that the proposed methodology can offer a systemic design guideline, simplified and methodical design procedure, and satisfactory the port isolation performance. To the authors' best knowledge, this is the first work that has applied the CM and DM theory to a dual-polarized antenna and is providing comprehensive results which consider the mutual coupling between two ports.

The remainder of this paper has been organized as follows. Section II presents the CM and DM theory for the advanced antenna design. In Section III, a design example of the dual-polarized antenna

has been reported with detailed design guidelines and antenna performance. In Section IV, a new perspective for comparing the performance, including the mutual coupling effect, has been reported with an active S-parameters analysis. Finally, Section V presents the conclusions draw from this study.

2.2. Principle of the CM and DM Theory

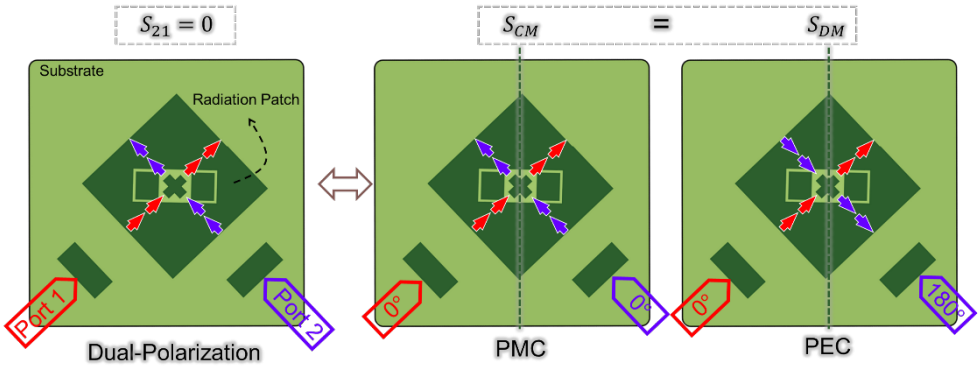

Figure 3. Sketch diagrams of a dual-polarized antenna and the corresponding current distributions on the radiation patch.

Fig. 3 shows a sketch diagram of an arbitrary dual-polarized antenna system. Because it is a dual-polarized antenna, the ports were designed to generate orthogonal currents for each path. The red and blue arrows in Fig. 3 represent the currents of each port. As is well-known, the objective of a dual-polarized antenna is to let $S_{21} = 0$ from the perspective of the single-ended and passive S-parameters to operate independently for increasing the data throughput. This can be achieved by utilizing the CM and DM theory, a new analysis method presented in this work. CM and DM refer to applying in-phase and out of phase signals, respectively, to each port in the two-port antenna system. Therefore, in CM, the same phase and power are generated at each port and the boundary at the center between the ports becomes a perfect magnetic conductor (PMC). In DM, similar to the CM, the power applied to each port is the same, but the phase difference is 180°, and the potential becomes zero at the center between the ports,

leading to occurrence of a boundary of a perfect electric conductor (PEC) [13]. The CM and DM S-parameters for the dual-polarized antenna system are as follows [14].

$$S_{CM} = (S_{11} + S_{12} + S_{21} + S_{22})/2 \quad (1)$$

$$S_{DM} = (S_{11} - S_{12} - S_{21} + S_{22})/2 \quad (2)$$

specifically, because the proposed dual-polarized antenna has a symmetrical and reciprocal two-port network, the equations satisfy the conditions S_{11} = S_{22} and S_{21} = S_{12}. The CM and DM S-parameters for the two-port antenna system are given below. Thus, the CM and DM S-parameters for a dual-polarized antenna system can be simplified as

$$S_{CM} = S_{11} + S_{12} \quad (3)$$

$$S_{DM} = S_{11} - S_{12} \quad (4)$$

combining (3) and (4), we get

$$S_{11} = S_{22} = (S_{CM} + S_{DM})/2 \quad (5)$$

$$S_{21} = S_{12} = (S_{CM} - S_{DM})/2 \quad (6)$$

from (5) and (6), it can be found that the isolation equation of S_{21} = 0 between the ports can be realized for $S_{CM} = S_{DM}$ when we consider the design of the dual-polarized antenna from the perspective of the CM and DM theory. In other words, for an arbitrary symmetrical and reciprocal dual-polarized antenna, if the CM and DM S-parameters are identical, the isolation between the ports can be successfully achieved. In addition, if the CM and DM S-parameters are close to 50 **Ω**, the matching condition is satisfied as well. This conclusion could provide a new insight into the design of the dual-polarized antenna, which will be discussed in detail in the following sections.

The following section presents an independently adjustable CM and DM theory-based methodology for and easier and more logical design, starting with the designing and determination of the antenna

dimensions in a target frequency band. Metal sticks were used to enable the air-filled substrate to satisfy the N78 band. Unlike other study, this method implements an air-filled substrate and allows the antenna to operate without an additional jig to fix the antenna. In addition, the desired field is realized by making structural changes using the metal sticks, and as a result, independently controllable performance for CM and DM analysis is obtained.

2.3. Design of the Dual-Polarized Antennas

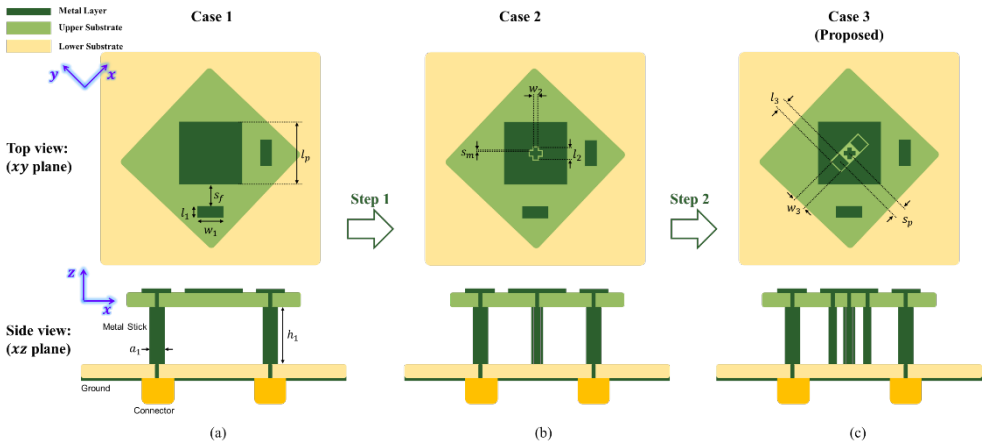

Figure 4. Evolution progress of the top and side views of the dual-polarized antenna, where w_1 = 5 mm, l_1 = 3 mm, s_f = 4 mm, l_p = 22 mm, a_1 = 2 mm, h_1 = 9.5 mm, s_m = 0.4 mm, w_2 = 1 mm, l_2 = 3 mm, w_3 = 2.6 mm, l_3 = 2 mm, s_p = 3 mm. (a) Case 1: Dual-polarized antenna without decoupling structures. (b) Case 2: with the cruciform metal stick for independently controllable CM only. (c) Case 3 (proposed): with the additional metal sticks for both independently controllable CM and DM.

The evolution progress of the dual-polarized antenna and the design parameters are proposed in Fig. 4 as the top and side views. As shown in Fig. 4(a), an air-filled substrate and indirect feed were used to achieve sufficient bandwidth to satisfy the N78 band. When an air-filled substrate was used, an appropriate bandwidth could be obtained using (7) from [19].

$$BW = \frac{96h\sqrt{\mu/\varepsilon}}{\lambda\sqrt{2}(4+17\sqrt{\mu\varepsilon})} \tag{7}$$

where ε and $h$are the permittivity and the thickness of the substrate, respectively. Considering these relationships, a thick and low-permittivity substrate is necessary for improving the bandwidth of the antennas. Typical substrates have a standard thickness and permittivity greater than 1, they limit the bandwidth of several

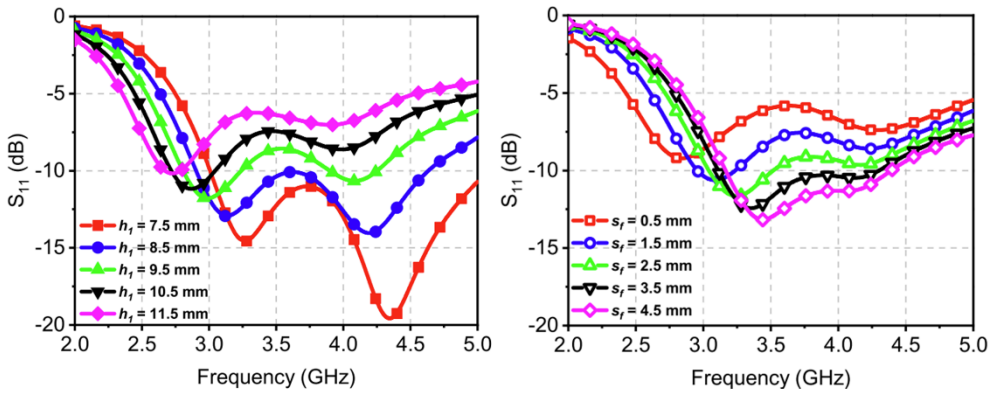

(a) (b)

Figure 5. Simulated reflection coefficient results with respect to different antenna geometry parameters. (a) shows the results at different heights, h1 and (b) shows the results at different values of the distance between the feeder and radiator s_f.

antennas. However, this limitation can be overcome by using an air-filled substrate which not only has no limitation on the thickness but also has a permittivity of 1. Thus, an air-filled substrate was achieved by using metal sticks on two sides, as shown in Fig. 4(a), because the metal sticks not only excite the patch but also fix the upper substrate. In addition, a coplanar capacitive feeder was used with the sticks connected by the via-hole. Additionally, even though using an air-filled substrate makes advantages when it comes to performance, the process complexity could be increased. The small rectangular copper traces on the upper substrate shown in Fig. 4(a) indirectly excited the patch for bandwidth improvement [20]. To control each mode steps 1 and 2 were proposed as illustrated in Fig. 4(b) and (c). the slot and metal stick were employed to effectively concentrate the electric field. Determining the dimension of the slot and the presence of the middle metal stick was important because the field can be weak if a slot is too big or the middle metal stick is absent. Fig. 4(b) has a cruciform slot, and the middle metal stick is connected to the metal layer of the upper

substrate through a via-hole (see side view). Similarly, Fig. 4(c) has additional metal patterns and sticks around the cruciform pattern.

2.3.1 Design Procedure

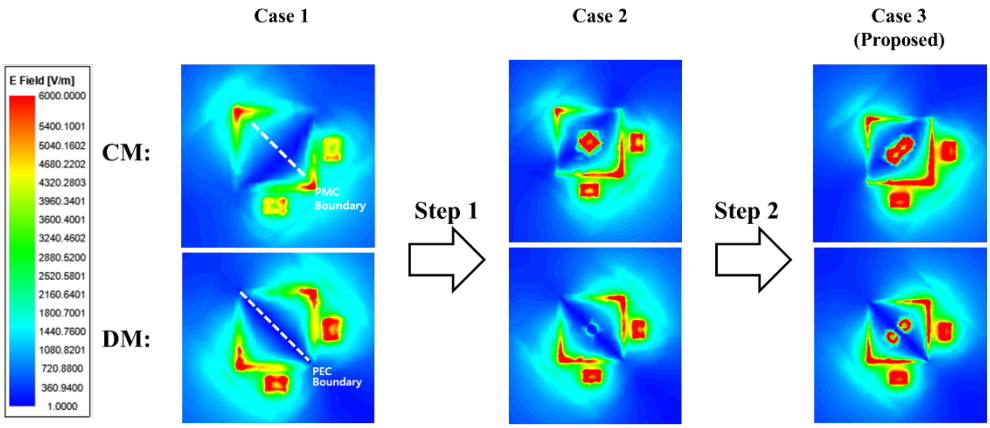

Figure 6. Electrical field distributions about CM and DM for (a) case1, (b) case 2, and (c) case 3 (proposed).

For appropriate operation, the antennas' bandwidth must be wide and matched adequately. So, the parametric study has been conducted as illustrated in Fig. 5. Especially, a higher value of $|S_{11}|$ is preferred because matching can be easily affected by some coupling. In addition, independent mode results were presented by adjusting parameter l_2 corresponding to the electric field added only in CM and s_p corresponding to the electric field added only in DM. Fig. 3(a) shows the change in the results when the height of the antenna is adjusted. As this method changes both poles, it was used to set the center frequency. Fig. 3(b) shows the result after adjusting the distance between the indirect feeder and the radiator. Unlike before, only one pole could be adjusted, which was used in the optimization process to satisfy the condition $|S_{11}| > 10$ dB. When looking at each result in Fig. 3(a) and (b), it can be seen that the matching deteriorates as the frequency decreases, and this can be resolved by adjusting the size of

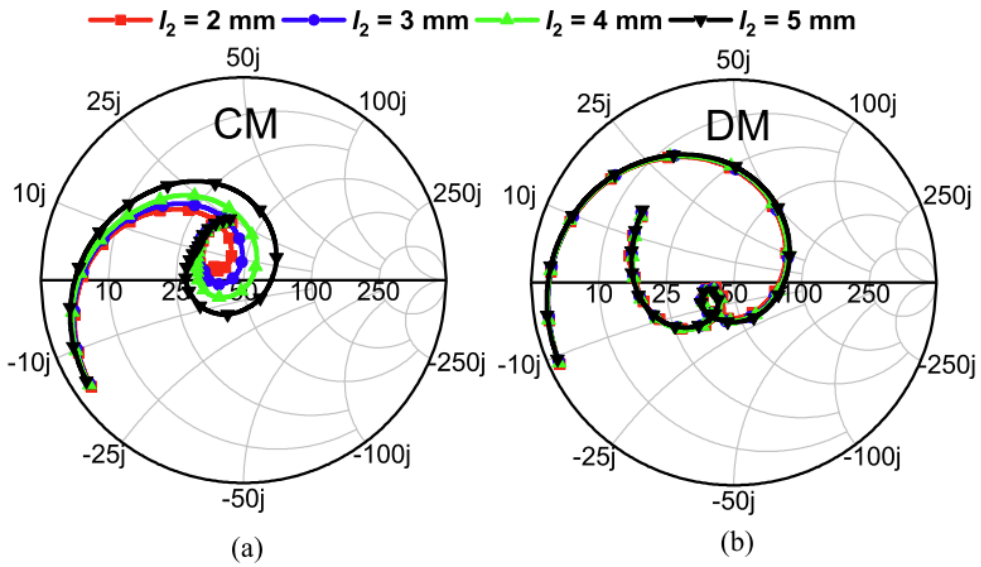

Figure 7. Smith charts of case 3 with respect to different l_2: (a) CM, (b) DM.

the radiation patch. In addition, two thin FR-4 substrates (thickness = 1.6 mm) were used; the upper substrate was used to laminate the coplanar feeding network and the radiation patch, whereas the lower substrate was used for the ground and connectors. A low-cost method was implemented using this typical process. First of all, it should be noted that the point where the two modes meet on the Smith chart so as to realize the isolation is the same frequency. For isolation between the ports, the design was carried out using the CM and DM analysis by performing the following two steps.

Step 1: A cruciform floating metal stick was inserted in the center of the radiator, as shown in Fig. 4(b). Owing to the center PEC boundary condition which created a zero voltage difference in the middle of the radiation patch for the DM, the electrical field distribution was almost unchanged by the additional metal stick as shown in Fig. 6(a) and (b). On the other hand, from these figures, it can be seen that the additional structure changed the electrical field distribution of the CM. Consequently, the trace of the smith chart for the CM could be

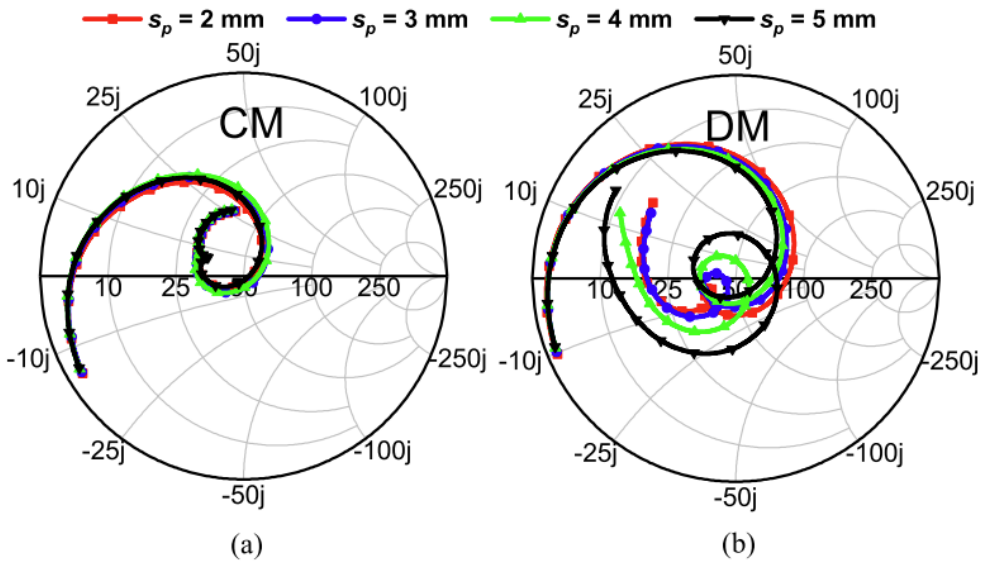

Figure 8. Smith charts of case 3 with respect to different s_p: (a) CM, (b) DM.

adjusted independently whereas the trace of the DM remained unchanged as shown in Fig. 7(a) and (b), which is for different values of l_2.

Step 2: The metal sticks were inserted further near the middle one as illustrated in Fig. 4(c). As a result, next to the middle metal stick, an additional structure created a strong electrical field distribution for the DM as shown in Fig. 6(c). On the contrary, owing to the extra metal stick close to the middle one, the electrical field distribution was similar to that in case 2. Therefore, the further metal sticks near the middle one could adjust DM impedance independently whereas the CM impedance remained unchanged as shown in Fig. 8(a) and (b). which is for different values of s_p.

2.3.2 Experimental Results

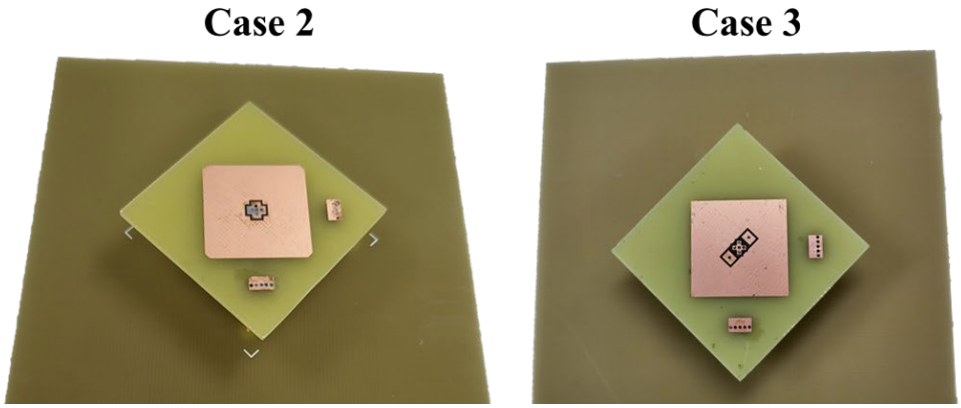

Figure 9. Photograph of the presented dual-polarized antenna corresponding to (a) case 2 and (b) case 3 (proposed).

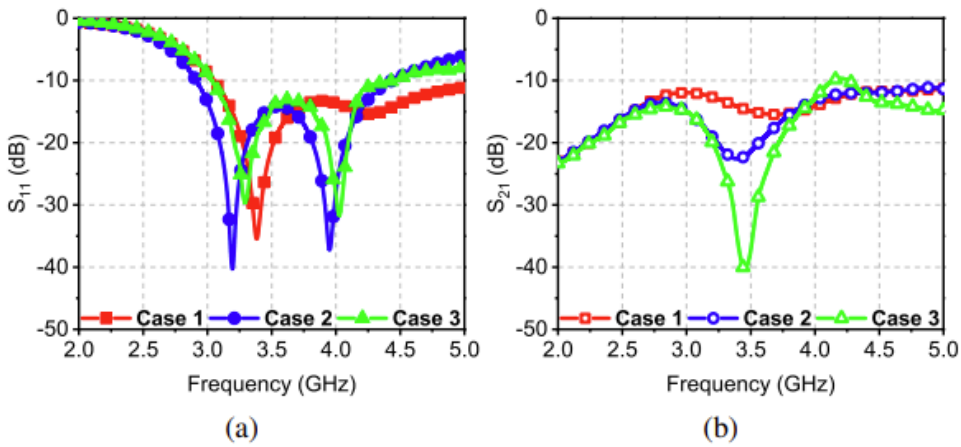

Figure 10. Measured (a) S11 and (b) S21 for case 1, case 2, and case 3.

To demonstrate the performance of the proposed dual-polarized antennas, a prototype was manufactured, as illustrated in Fig. 9(a) and (b). The two FR-4 substrates were connected by soldering metal sticks, and two 50 Ω SMA connectors were employed beneath the ground plane for the antenna test. Fig. 10(a) and (b) indicate the measured results for S11 and S21 according to the corresponding cases. In each case, it can be seen that the condition $|S_{11}| > 10$ dB is satisfied from 3.3 to 3.8 GHz, as shown in Fig. 10(a). However, as

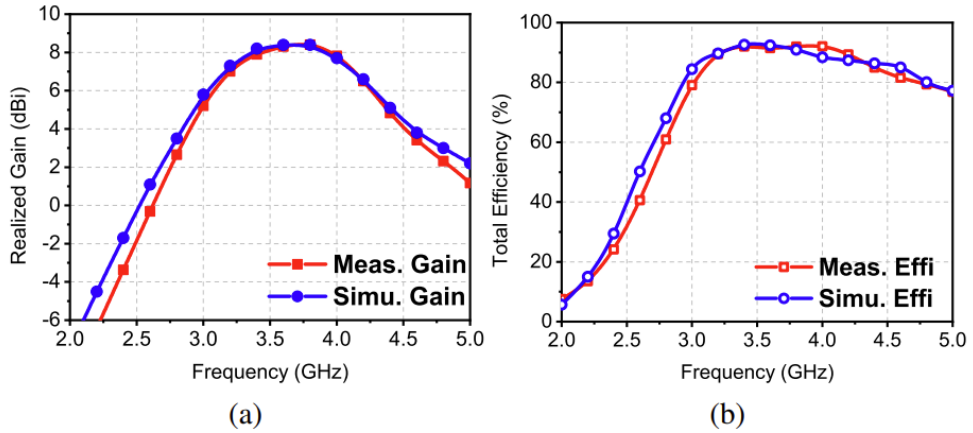

Figure 11. Simulated and measured (a) realized gain and (b) total efficiency of the proposed dual-polarized antenna.

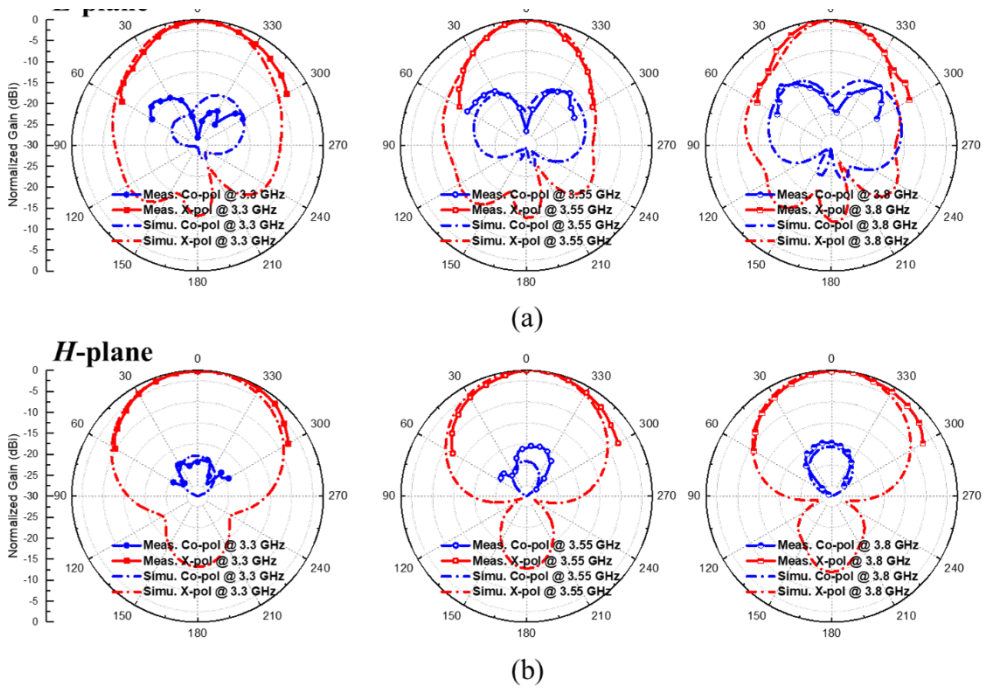

Figure 12. Simulated and measured (a) *E*-plane and (b) *H*-plane at 3.3, 3.55, and 3.8 GHz.

illustrated in Fig. 10(b), the original isolation between the ports is approximately 15 dB when the proposed methods are not used. On the other hands, isolation is progressively improved by implementing the CM and DM. When only the DM is controlled, the isolation is 20 dB,

and when both the CM and DM are independently adjustable, isolation of up to 40 dB is achieved through a more delicate design. In other words, a novel design methodology for dual-polarized antennas was realized by simply adding the multi-functional metal sticks.

The simulated and measured realized gains and efficiencies are shown in Fig. 11(a) and (b), respectively. Across the target band (from 3.3 to 3.8 GHz), the simulated realized gain is 8-8.4 dBi, whereas the measured value is stable at 8 dBi. In addition, the simulated total efficiency is 88-92%, whereas the measured value is 90-92%. The low loss from the air-filled substrate and the property of good impedance matching contribute to the high performance of the antenna, even though the FR-4 substrate has a high loss tangent. As a result, the matching and isolation conditions are satisfied for the N78 band, and the realized gain and total efficiency are approximately 8 dBi and 90%, respectively. Moreover, it is possible to achieve the same performance for each frequency by obtaining a constant value result in the target band.

The simulated and measured *E*- and *H*- planes normalized radiation patterns obtained by feeding the signal through a port, and with the other end terminated by a 50 **Ω** resistance, are illustrated in Fig. 12(a) and (b), respectively. The radiation patterns are symmetrical between the two ports and have thus not been shown for brevity. As can be seen from the figure, a pattern with low cross-polarization (the maximum is approximately 30 dB) in the broadside direction is realized in both planes from 3.3 to 3.8 GHz. In addition, it has a stable radiation pattern for each presented frequency, and the measured and simulated results agree well.

2.4. Intensive Interpretation

This section provides a comprehensive and in-depth analysis of dual-polarized antennas to reflect effect of practical requirements on the results. The studies reported thus far have only verified the isolation and XPD between the ports with the design methods for dual-polarized antennas. However, since a dual-polarization antenna operates independently, simultaneous operations must be considered. In this study, new issues regarding the active S-parameter analysis have been presented by considering the coupling effect and beam pattern distortion due to moderate XPD. Rather than evaluating the antenna performance at an S-parameter level using the proposed concept, it is expected that the optimal performance for the desired application can be achieved by considering the practical conditions.

2.4.1 Active S-parameters

The active S-parameter is calculated as follows [21]:

$$Act.S_{porti} = \sum_{j=1}^{n} S_{ij} \frac{a_j}{a_i} \tag{8}$$

Where S_{ij} is the passive (typical) S-parameter under the terminated conditions. a_j is the complex excitation coefficient of port j, which includes an amplitude and a phase. Since dual-polarized antennas consist of two ports and reciprocal systems, (8) can be modified as follows:

$$Act.S_{port1} = Act.S_{port2} = S_{11} + \Delta A \times e^{j\Delta\phi} S_{12} \tag{9}$$

where ΔA and $\Delta\phi$ are the amplitude ratio and the phase difference between the ports, respectively. As shown in (9), when both ports are excited, S_{11} can be affected by the amplitude ratio, the phase difference between the ports, and S_{21}. This can also be interpreted as a physical insight. If we consider the matching of two antennas

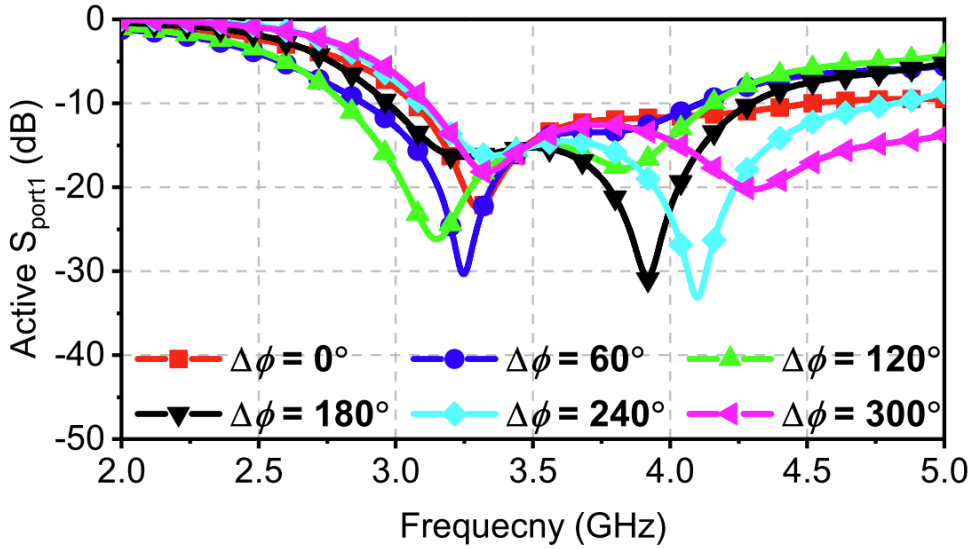

Figure 13. Measured active S_{port1} with respect to the different phase difference, maintaining the amplitude ratio as 1.

operating independently, the inherent matching conditions and coupling levels affect the result. Further, the power and phase of the adjacent element also influence the result; as the power increases, the specific phase that cause the in-phase between S_{11} and S_{21} deteriorates the result.

Fig. 13 shows that the active S-parameter changes in port1 when a phase difference is introduced under the condition that the same power is excited to each port as $\Delta A = 1$. In viewing the results of the method above and referring to the S-parameter results shown in Fig. 10(a) and (b), it can be seen that the results for different values of the phase difference satisfies the matching condition of $|S_{port1}| > 10$ dB from 0° to 360° under considering the coupling effect. In other words, when the same power is supplied between each port, the dual-polarized antenna operates as intended.

Fig. 14 shows that the results of the proposed antenna performance are affected in the situation where ΔA and $\Delta\phi$ change simultaneously

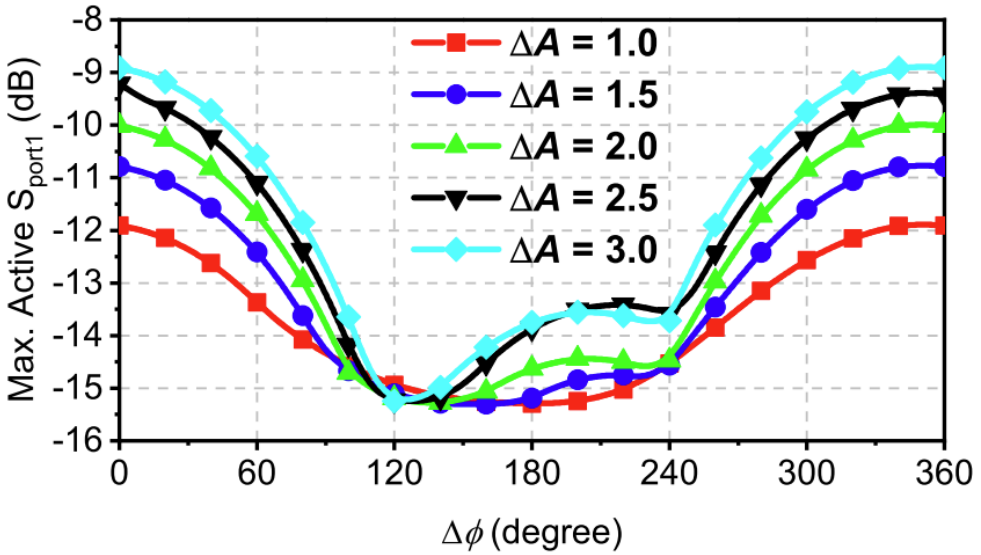

Figure 14. Measured maximum active S_{port1} from 3.3 to 3.8 GHz considering possible amplitude ratio and phase difference for practical conditions.

across 3.3 – 3.8 GHz in realistic scenarios. If all graphs are plotted for each change simultaneously, it is difficult to recognize and they take up a lot of space. Therefore, in this study, the method of finding the maximum value of the active S-parameter in N78 band was specifically chosen. The x-axis reflects the range of the phase difference and the overlapping graphs with different ΔA value demonstrate the change in the applied amplitude ratio. As a result, it can be seen that as ΔA increases, the coupling increases and the matching level deteriorates as ΔA increases, as can be interpreted by (9) as well. Interestingly, looking at the results, the matching condition improves when the phase difference is approximately 180° and deteriorates when the phase difference is approximately 0°. This is intuitive because the coupling adds up S_{11} and reduces it in the opposite situation because the other ports are close to each other owing to the characteristics of the dual-polarized antenna. However, the corresponding intuitive analysis can only be applied to dual-polarized antennas, and if there is a distance of 0.5λ such as an array antenna, the interpretation can be different

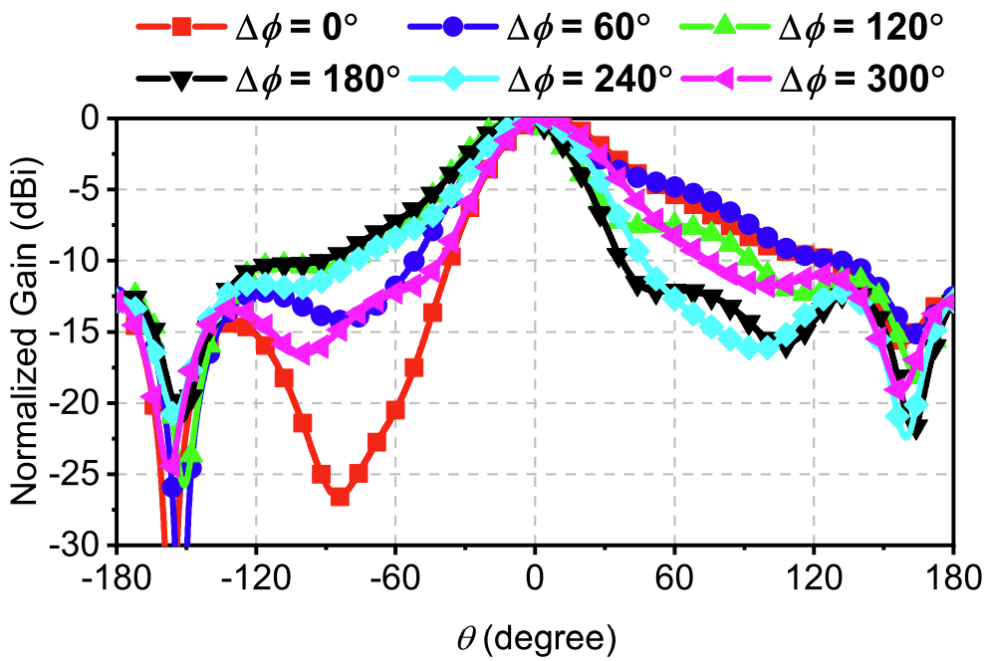

Figure 15. Simulated normalized beam pattern at 3.6 GHz with respect to the different phase differences, maintaining the amplitude ratio as 1.

because S_{11} and S_{12} also have phases. To summarize the analysis, in the proposed dual-polarization antenna, when each port operates independently, considering the $|S_{port1}| > 10$ dB matching condition, the amplitude ratio can be used up to $\Delta A = 2$ in all phase difference sequences.

Fig. 15 shows the beam pattern distortion and changes according to the phase difference at 3.55 GHz with $\Delta A = 1$. The proposed antenna exhibits an XPD of 20 dB. The results indicate that the beam pattern exhibits an error of $\pm 6°$ for all possible phase sequences. It should be noted that even the XPD level which many previous studies have targeted [22], has a noticeable negative performance impact. In future work, it is hoped that these results will be reflected, and more reliable results will be obtained.

2.4.2 Cross-Polarization Discrimination (XPD)

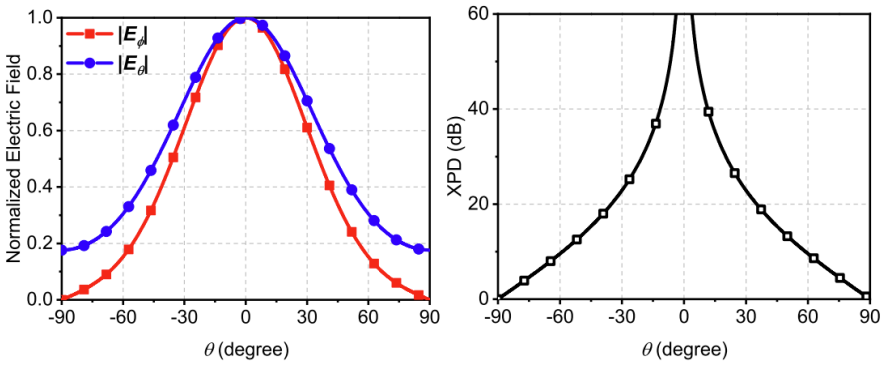

(a) (b)

Figure 16. Calculated (a) electric pattern factors and (b) XPD.

In [23], the analysis of XPD based on the electric field equations for slant dual-polarized antenna has been proposed. Although the reported paper was developed based on the dipole, the method could be effective here. So, this paper was developed based on the electric field of the path antenna because patch-type radiation was used. The electric field of $\pm 45°$ polarized antennas could be defined as follows:

$$E_{+45°}(\theta) = E_\theta \cos 45° + E_\phi \cos 45° \quad (10)$$

$$E_{-45°}(\theta) = E_\theta \cos 45° - E_\phi \cos 45° \quad (11)$$

where E_θ and are E_ϕ the θ and ϕ components of electric pattern factor in the far-field region, respectively. Here, we assume that $E_{+45°}$ is the Co-polarization and is $E_{-45°}$ the Cross-polarization, and be defined as a function of θ.

$$XPD(\theta) = 20 \log(E_{+45°}(\theta)/E_{-45°}(\theta)) \quad (12)$$

by the equation, E_θ and E_ϕ must be equal to achieve high XPD. According to the classical antenna theory [23], to analyze the degradation of XPD with respect to increase θ, the electric pattern factors in the far-field region can be derived as follows, in the form of a function of θ the plane of $\phi = 45°$.

$$E_\theta(\theta) = E_0 \cos\phi \frac{\sin\psi}{\psi} \cos(\frac{kL}{2} \cos 45° \sin\theta \cos\phi) \quad (13)$$

TABLE I
ANTENNA PERFORMANCE COMPARISON TABLE

Ref.	Method	Frequency (GHz)	Profile	Isolation (dB)	XPD (dB)	Total Efficiency (%)	Gain (dBi)
[9]	Suspended patch	2.9-4.3	0.15λ	>30	26	-	-
[10]	Bow-tie dipoles	3.2-3.9	0.16λ	>40	25	-	-
[12]	Open-loop resonators	3.2-3.7	0.07λ	>38	33	-	-
[22]	Parasitic loops with dipoles	1.8-2.6	2.5λ	>35	30	85	8.5
[24]	H-shaped slot	3.1-3.8	0.12λ	>43	40	85	8.1
[25]	Magneto-electric dipoles	3.3-4.2	0.25λ	>30	25	90	8.2
[26]	Crossed straight dipoles	1.7-2.9	0.25λ	>28	20	-	8.5
[27]	Vector synthesis	3.3-3.6	0.21λ	>26	25	90	8
This work	Mode segmentation using metal sticks	3.3-3.8	0.14λ	>20	20	90	8

$$E_{\phi}(\theta) = E_0 \cos\phi \sin\phi \frac{\sin\psi}{\psi} \cos(\frac{kL}{2} \cos 45° \sin\theta \cos\phi) \quad (14)$$

$$\psi = \frac{kL}{2} \cos 45° \sin\theta \sin\phi \quad (15)$$

where k is the usual free-space phase constant. In general, the length of path antenna is designed with a length of $L = 0.5\lambda$. The electric pattern factors of (13) and (14) can be expressed as Fig. 16(a). The red and blue lines are the absolute values of electric pattern factors about each component (i.e., $|E_{\theta}|$ and $|E_{\phi}|$), respectively. Fig. 16(b) reveals the result of normalized XPD form the induced patter factors. As a result, the XPD is degraded with increasing the angle $|\theta|$ based on the theoretical analysis.

Table I shows a comparison of the performance of the proposed dual-polarized antenna with other recently reported works on antennas. In the table, λ is the free-space wavelength at the central operating frequency. It can be seen that the proposed antenna exhibits excellent performance based on the corresponding information. It was designed based on the analysis of a higher hierarchy, and a wide bandwidth was obtained. In addition, high efficiency and gain were achieved despite the use of an FR-4 substrate. The results corresponding the design in this work are comparable to those reported in the literature when it comes to the isolation and XPD values.

Chapter 3. Isolator Design

3.1 Introduction

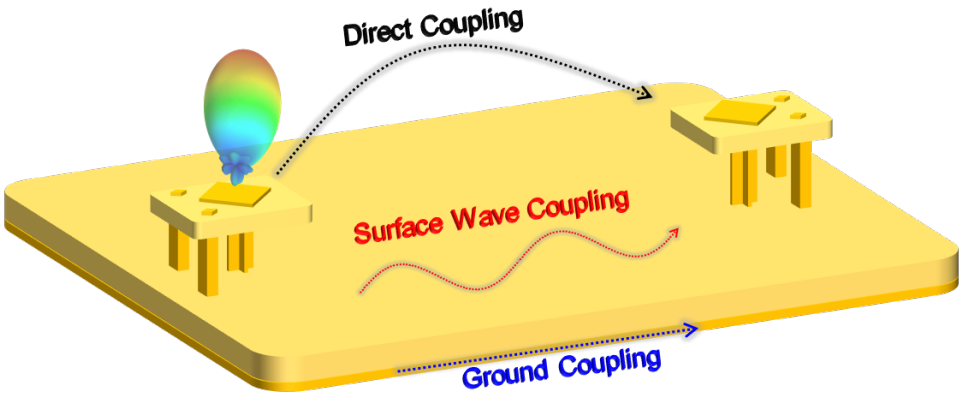

Figure 17. Schematic of two-element array and coupling path between the antennas.

Recently, wideband and dual-polarization characteristics have been more important to obtain a high data throughput owing to the enormous amount of signal processing required for sub-6 GHz. Meanwhile, as the abovementioned on the background, to eliminate a coupling between the transmitter and receiver has been a key technique for the advanced system. So many researchers have focused on decoupling methods. Among the reported approaches for mitigating mutual coupling, decoupling surface using the interaction between direct coupling and the wave reflected by the surface [28], the transmission line based method [29], the resonance patter [30], metasurface [31], resistive films [32], side walls [33], common and differential mode cancelation [15], and electromagnetic band-gap (EBG) [34] are the well-known used as isolation methods. In [35], mutual coupling between dual-polarized array antennas has improved

using an array antenna decoupling surface (ADS). Here, the ADS was optimized and designed for single-polarized array antennas, and good results were obtained by the method. However, the isolator has some limitations when it is applied to dual-polarized array antennas. Moreover, although multiple-input multiple-output (MIMO) systems that use dual-polarization and increase array configurations have recently been in the spotlight, the isolator still has the abovementioned limitations as revealed in an earlier study. For instance, in [36], an isolator notch was obtained using resonant structure. However, it was hard to improve all dual-polarized array configurations. As seen in the results, S_{25} did not have an isolation notch, and S_{26} deteriorated despite the isolator being in use. Therefore, in this paper, to reduce the mutual coupling between Tx and Rx using a dual-polarized array antenna, as illustrated in Fig. 17, the coupling paths are first identified. Then, a new effective hybrid structure is presented and demonstrated, maintaining a high isolation level with the devised antenna featuring bandwidth improvement and dual-polarization characteristics along with a novel concept of using versatile metal sticks.

3.2 Design of Decoupling Structure

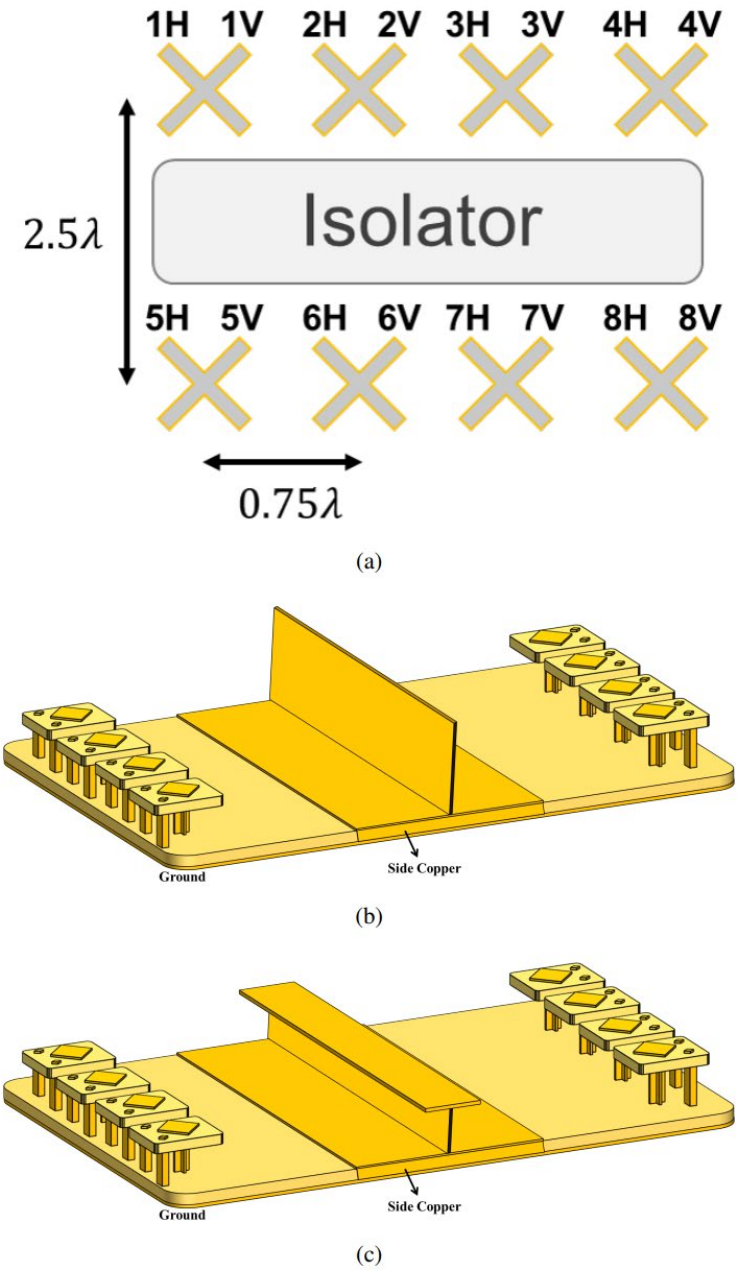

Figure 18. (a) Layout and numbering scheme of an array configuration of IBFD operation; 3D view of the single wall: (b) straight and (c) bent.

This section describes the analysis of the decoupling method of the array antennas for two sets of 1×4 antenna arrays using metallic walls. First, the corresponding results were investigated using the

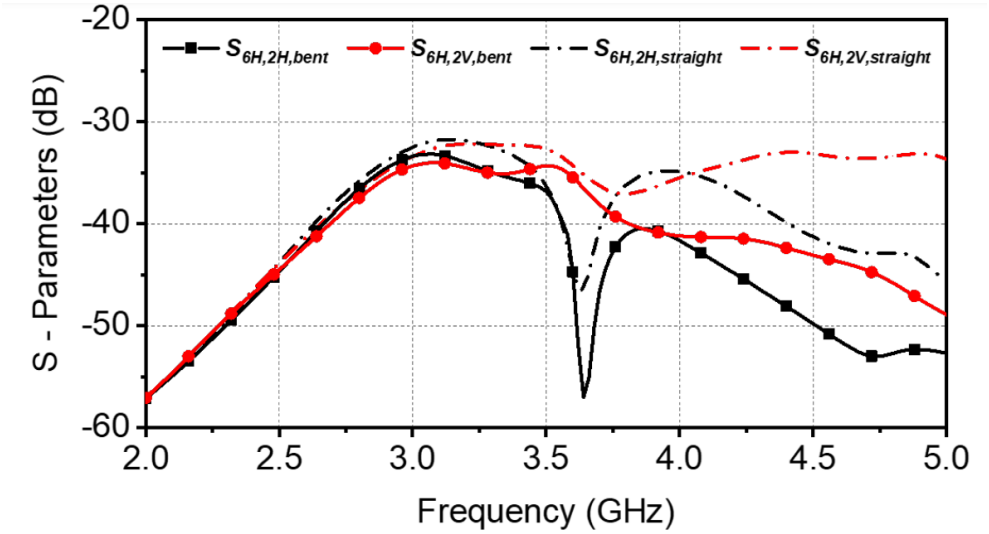

(a)

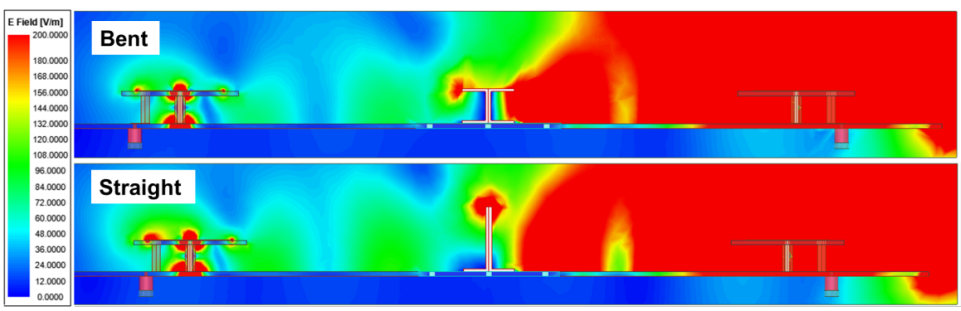

(b)

Figure 19. Simulated results with respect to the shape of the wall: (a) $S_{6H,2H}$, $S_{6H,2V}$; (b) electric field distribution.

electric field distributions for straight and bent shapes on a single wall. Thereafter, the results were obtained according to the number of walls, and the optimal number of walls for the system was determined.

The path that causes coupling is analyzed as illustrated in Fig. 17, and the isolator used to implement the decoupling performance is described. Coupling can be analyzed through categorization into direct, surface waves, and ground couplings. This paper proposes a method for identifying and solving the coupling in dual-polarized array antennas based on this approach.

3.2.1 Wall Analysis

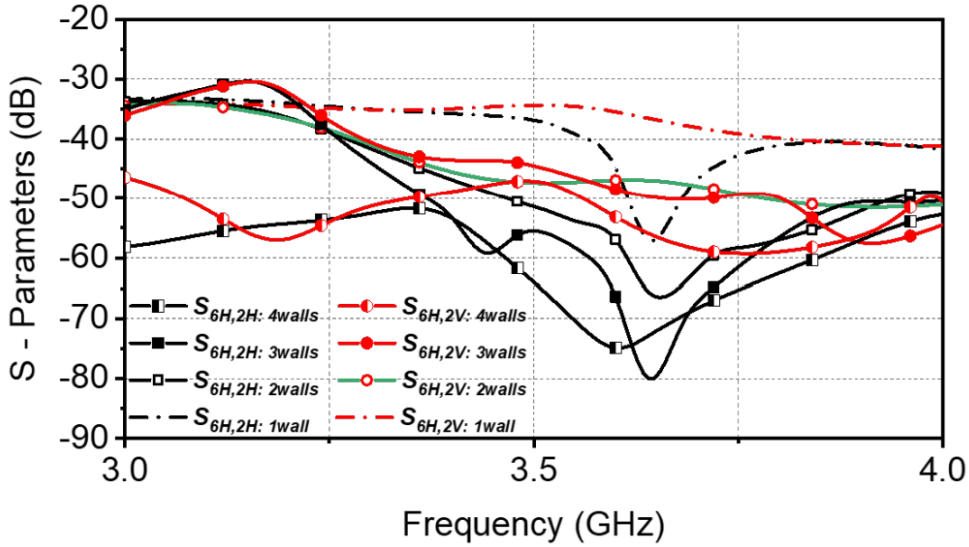

(a)

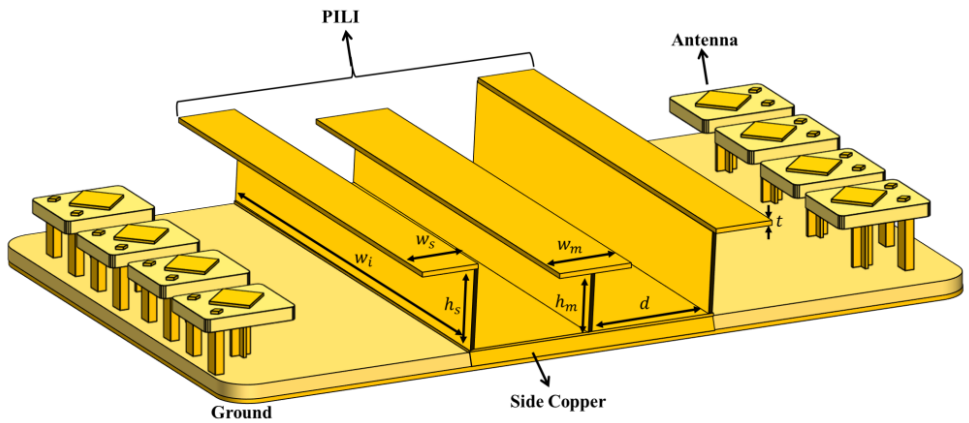

(b)

Figure 20. (a) Simulated $S_{6H,2H}, S_{6H,2V}$ with respect to the number of walls; (b) 3D view of the system with a PILI, where w_s = 12 mm, h_s = 11 mm, w_m = 18 mm, h_m = 9 mm, w_i = 290 mm, d = 20 mm, and t = 1.5 mm.

Fig. 18(a) shows the numbering and layout of the Tx-Rx array antenna system. The transmitter and receiver were each set with four antennas. Therefore, these are referred to as two sets of 1×4 arrays.

Antennas belonging to the same set were arranged at a spacing of 0.75λ; the distance between the sets was 2.5λ, and isolators were presented between them. This study focused on improving the isolation between the upper set (1 – 4 H, V) and the lower set (5 – 8 H, V). The proposed isolator, which has a metallic wall structure that intuitively suppresses direct coupling, is shown in Fig. 19(b). In addition, a planar inverted-L isolator (PILI), three metallic walls) was connected to the ground of the main substrate through via holes and a side copper. Ground coupling can be suppressed by operating the isolator as a resonance structure through PILI using the transmission line analysis method. Fig. 18(b) and (c) illustrate the 3D models with straight and bent shapes for a single wall isolator, which is the unit structure of PILI. The straight wall height was set to λ/4 to eliminate ground coupling, and the corresponding analysis is being described in next section. Likewise, the height of the bent-shaped wall was determined. Because the physical lengths of the bent and straight shapes must be the same, the bent shape was implemented with a low profile, as in the 3D model illustrated in Fig. 18(c).

Fig. 19(a) shows the simulation results of S-parameters; the coupling level of Tx-Rx can be determined numerically. The bent structure improves the isolation of both the horizontal and vertical polarizations. These results can be explained based on the field distribution presented in Fig. 19(b), plotted as a complex magnitude for the time and period independent results. The field passing from Tx to Rx was further induced downward because of the curved edge caused by the bent shape. Therefore, diffraction is suppressed and the field intensity transmitted to Rx is reduced.

Fig. 20(a) reveals the results obtained by increasing the number of walls for each polarization. Intuitively, the number of walls in PILI

is significant because the walls can block direct coupling and prevent ground coupling simultaneously while adjusting the appropriate wall length. The black line represents the result of the same polarization when the number of walls increases, and the red line represents the coupling results of the two antennas with different polarizations. When considering the coupling between antennas with the same polarization, the isolation level proportionally improved as the number of walls increases. This tendency was also observed in the coupling results of the antennas with different polarizations. However, when the number of walls is three or more, the isolation level does not improve significantly. Thus, considering the area occupied by the isolator, the optimum number of walls to be used was three. Fig. 20(b) illustrates PILI's 3D model and dimension parameters determined based on next sections.

3.2.2 Transmission Line-Based Analysis

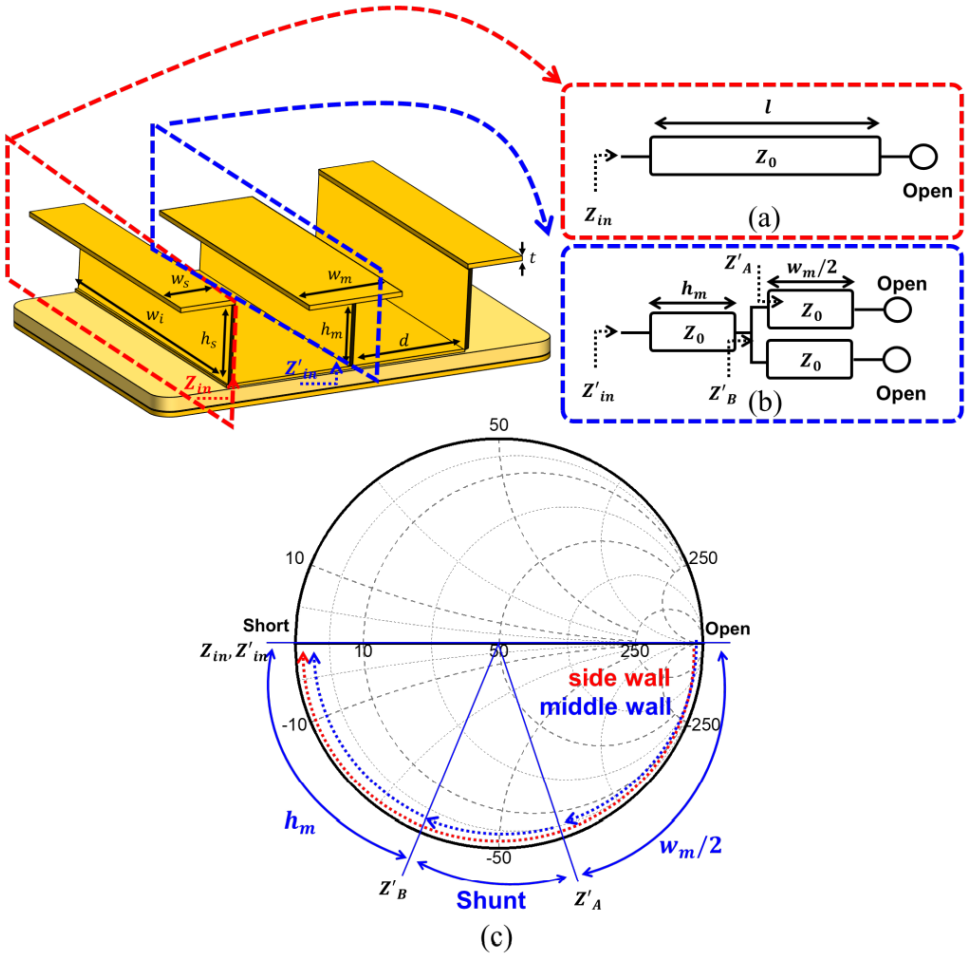

Figure 21. Description of the input impedance of a single wall analyzed as a transmission line: (a) side wall, (b) middle wall, and (c) Smith chart traces of each wall.

Because the presented distance condition among the array set is sufficiently large, the isolator satisfies the far-field condition. Therefore, the isolation wall could be modeled as a transmission line, as shown in Fig. 21(a) and (b), because the wave on the ground is a quasi-TEM. The input impedance of the side wall, based on the transmission line theory of the wall is as follows:

$$Z_{in} = Z_0 \frac{Z_L + jZ_0 \tan \beta l}{Z_0 + jZ_L \tan \beta l} \tag{16}$$

$$l \approx h_s + w_s \tag{17}$$

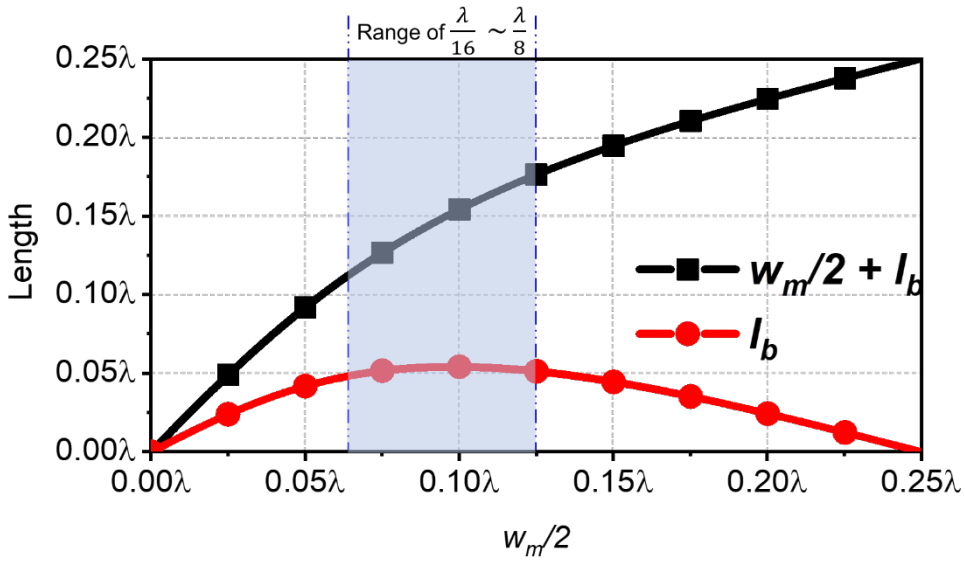

Figure 22. The results of the effective length by the shunt impedance decrease.

$$Z_{in} = \frac{Z_0^2}{Z_L} \tag{18}$$

where Z_0 and Z_L are the characteristic and load impedances of the walls, respectively. In addition, the line length is approximately represented by (17) because the walls' height could be modeled as a transmission line. Here, (18) is obtained if l is a quarter-wavelength. From the equation, Z_{in} can have a very low impedance if the load is high enough, and $Z_0 \ll Z_L$ is satisfied because the width of walls was sufficiently wide with w_i = 290 mm. The middle wall is composed of a T-shape for structural symmetry of the isolator; therefore, it is modeled as a shunt transmission line with w_m length and connected to the transmission line with h_m length. Interestingly, unlike the side wall, it satisfies the equation below because the shunt line decreases the additional impedance.

$$\frac{w_m}{2} + l_b + h_m = \frac{\lambda}{4} \tag{19}$$

where l_b is the effective length of the impedance decrease by the

shunt transmission line, which is identical to the shunt range in Fig. 21. Furthermore, (17) can be simplified under the condition that $w_m/2 = h_m = \Phi$ and $l_b \approx \lambda/20$. The approximation of l_b could be explained by an effective length from the shunt impedance decrease. The impedance is obtained by (16) with $Z_0 \ll Z_L$ and calculated as below.

$$Z_A' = \frac{Z_0}{j \tan \beta \frac{w_m}{2}} \tag{20}$$

$$Z_B' = \frac{Z_0}{j\, 2\tan \beta \frac{w_m}{2}} = \frac{Z_0}{j\, 2\tan \beta\left(\frac{w_m}{2}+l_b\right)} \tag{21}$$

the effective length by the shunt impedance decrease can be induced using the impedance calculated by (21).

$$\frac{w_m}{2} + l_b = \frac{1}{\beta}\tan^{-1}\left(2 \tan \beta \frac{w_m}{2}\right) \tag{22}$$

the result of (22) is illustrated in Fig. 22. Here, the condition of λ/16 to λ/8 range for $w_m/2$ is determined to maintain the constant shunt impedance decrease. As a result, l_b can be approximated by λ/20 as illustrated 22. In addition, the modified result about Φ is given below.

$$\Phi \approx \frac{\lambda}{10} \tag{23}$$

Accordingly, the dimensions of the middle wall are properly determined for resonance and must be smaller than the side wall. Consequently, the corresponding wall height can minimize the input impedance because the end edges of PILI are considered open circuits (OCs). This consideration is because the end of the line is in contact with air, which has an intrinsic impedance of 120π (377Ω).

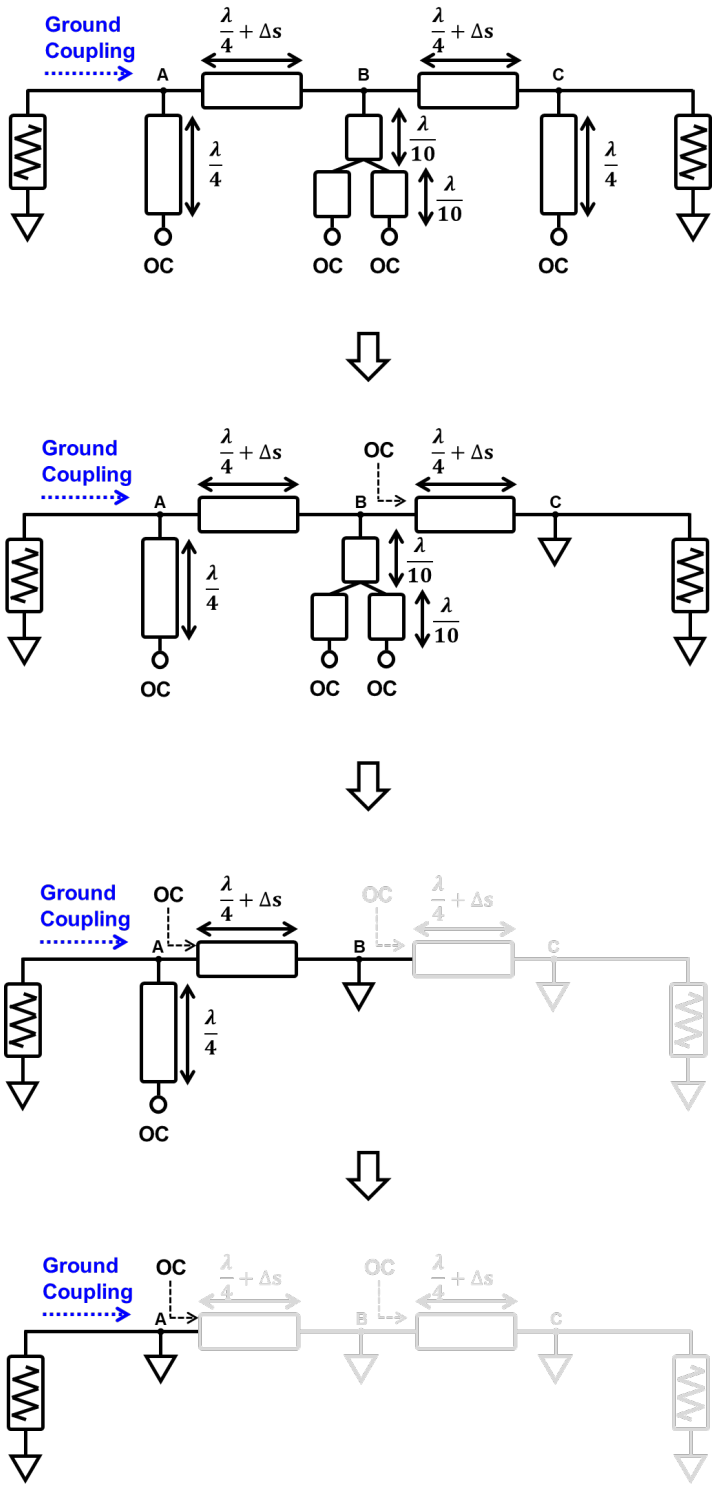

Figure 23. Schematic and analysis of triple-wall based on transmission line theory.

Fig. 23 shows the operating principle of PILI and ground signal

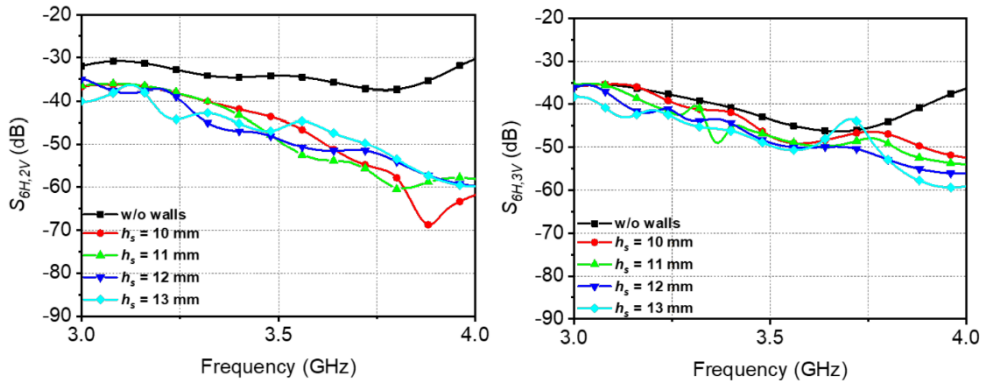

Figure 24. Simulated results with respect to different h_s values: (a) $S_{6H,2V}$ and (b) $S_{6H,3V}$.

flows based on transmission line analysis. Each wall can be interpreted as a single line through which the ground coupling passes, and the height and spacing of the walls are modeled as transmission lines. To begin the analysis in the process depicted in Fig. 23, the nodes where each line crosses are denoted by A, B, and C, respectively. When the length of the line from node C is λ/4, based on transmission line theory, it becomes a short circuit. Subsequently, it can be interpreted as an open circuit when looking at node C from node B because the spacing of the wall is λ/4. Δs is introduced to reflect differences from each array placement which make the different effective length for each path. The factor affects a few changes in isolation notches but was not dominant because the bandwidth of notches is wider than the effect of the difference for each array path. So, we resolved a minor mismatch through several parametric studies using HFSS simulation.

Moreover, the line of node B whose length is λ/5 becomes a short circuit, as illustrated Fig. 21(c). Subsequently, the same process is followed for nodes B and A. Finally, a short circuit exists in node A such that all ground coupling is induced to the walls by the low

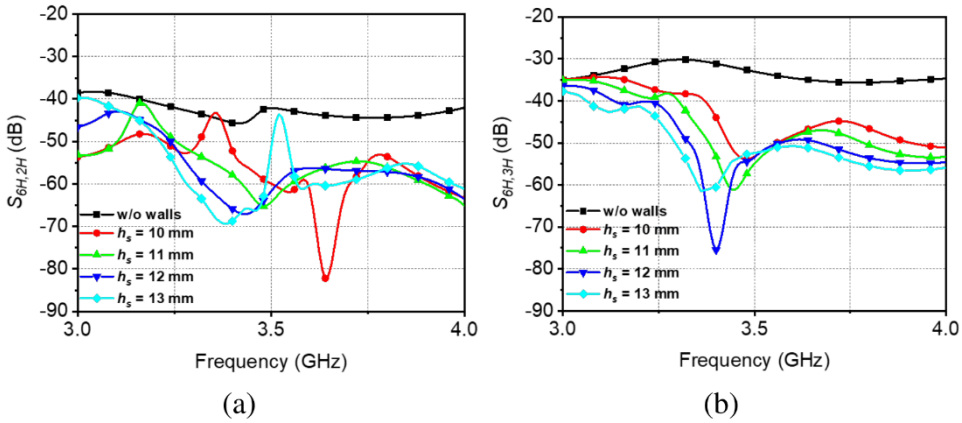

Figure 25. Simulated results with respect to different h_s values: (a) $S_{6H,2H}$ and (b) $S_{6H,3H}$.

impedance, which improves the isolation level. In summary, if metallic walls are used to realize PILI, direct coupling can be intuitively removed, and if the appropriate length and spacing are used when the walls of the PILI are connected to the ground directly through the side copper or via holes: the operation of the isolator can also be used as ground coupling suppression that acts as a resonance structure.

Before discussing the analysis, we explain the overall results based on a representative analysis of $S_{6H,2H}, S_{6H,2V}, S_{6H,3H}$, and $S_{6H,3V}$ rather than analyzing each antenna and polarization. Fig. 24 shows the results for $S_{6H,2V}$ and $S_{6H,3V}$. The overall isolation levels have improved by the addition of metallic walls. However, the variation in the resonance point with respect to the adjustment of h_s is not clear and irregular. This means that the ground coupling suppression does not work well for the polarization and the PILI only suppresses the direct coupling. Thus, an isolation level of approximately 50 dB was obtained in the absence of an isolation notch owing to the PILI at 3.5 GHz. By contrast, as illustrate Fig. 25, the presence of isolation notches owing to the isolator have improved the decoupling level at the target frequency. The results indicate that the resonance

frequency of the isolation notch caused by the isolator decrease as h_s increases because the increase in h_s leads to an increase in the electrical length of the metallic wall as depicted in Fig. 23, i.e., reducing the resonance frequency. In other words, the horizontal polarization results presented in Fig. 25 indicate that the isolator using the walls not only suppress the direct coupling but also effectively suppresses the ground coupling through the resonance structure, unlike the result in the case of the vertical polarization illustrated in Fig. 24.

Finally, for the coupling results from the vertical to horizontal polarization, it can be predicted that there is no significant improvement by suppressing the ground coupling and direct coupling using the isolator because of the continued existence of surface wave coupling. By contrast, a highly improved isolation level can be obtained by the suppressing the ground and direct couplings about the identical polarizations.

3.2.3 Isolator with EBG

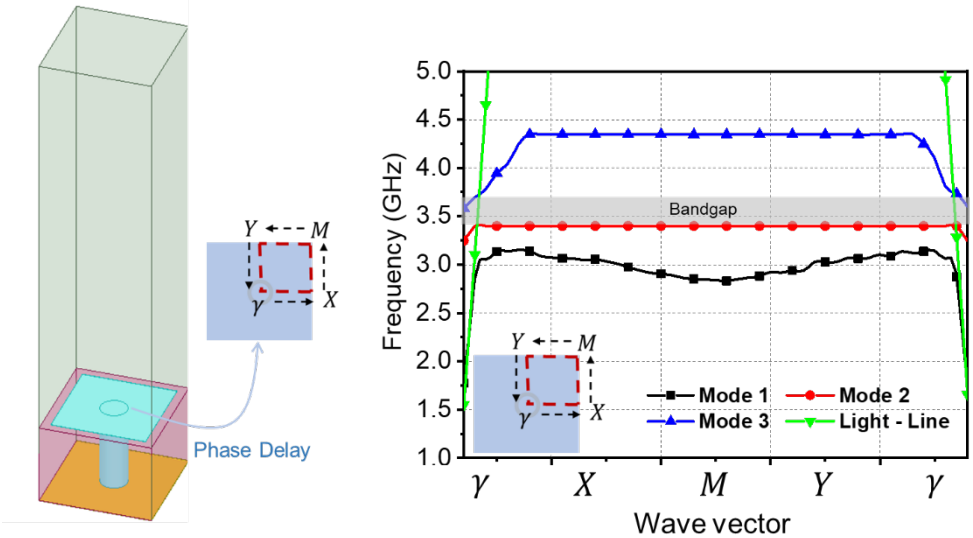

Figure 26. 3D model for periodic analysis and the resultant dispersion diagram.

To understand why different results for the polarizations correspondence identified above were obtained due to the surface wave coupling, an EBG that suppresses surface waves was implemented. To adequately anticipate the stop-band characteristic for the surface wave, a full-wave analysis using ANSYS HFSS is required. In the structure with 2-D periodicity using the unit cell symmetry, a dispersion diagram depicting the energy band of the EBG was obtained (refer to Fig. 26). Therefore, the unique propagation vector was grouped in a region referred to as the irreducible Brillouin zone [36], as indicated by the rectangular Γ, X, M, and Y in the inset of Fig. 26. The dispersion diagram presents the results for the three modes and a nondispersive light line. The slope of the graph is the inverse of the group delay because the frequency is differentiated with respect to the phase. This concept implies that the energy exists where there is a gradient, and the absence of a gradient or operation

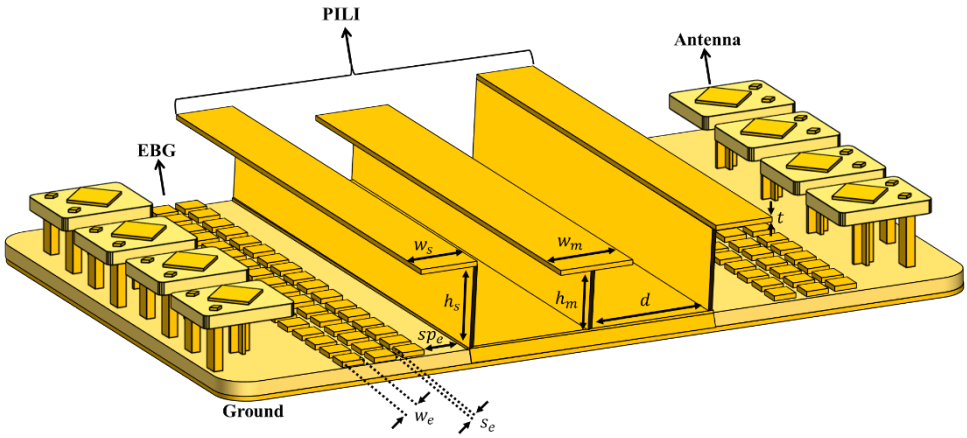

Figure 27. 3D view of the system with PILI and EBG, where w_s = 12 mm, h_s = 12 mm, w_m = 18 mm, h_m = 9 mm, d = 20 mm, t = 1.5 mm, w_e = 11.6 mm, s_e = 1 mm, and sp_e = 12 mm.

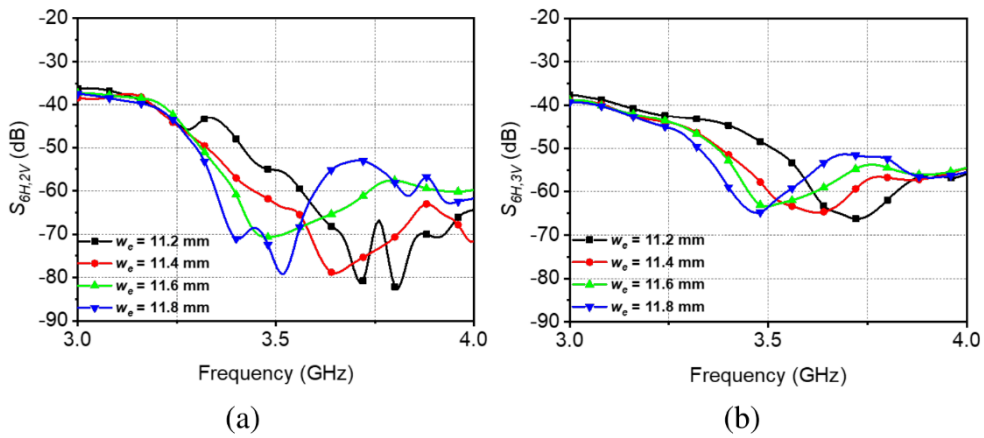

Figure 28. Simulated results with respect to different w_e values: (a) $S_{6H,2V}$ and (b) $S_{6H,3V}$.

outside the light line implies the absence of energy. Based on this concept, it is seen that there is a band-gap where the energy does not exist, represented in Fig. 26. As a gray region, and the surface energy analysis indicates that the corresponding part will play a role in suppressing the surface wave.

Fig. 27 illustrates the PILI arrangement, a wall structure that suppresses the direct and ground couplings and the EBG, which

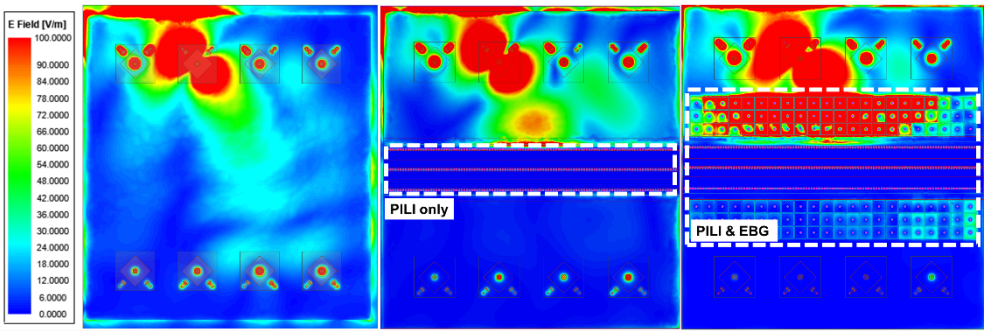

Figure 29. Electric field distribution of the array antenna system. (a) without the isolators, (b) with the PILI, and (c) with the PILI and EBG.

suppresses the surface wave coupling. The EBG was planted on the main substrate which shared the ground among the array antenna sets, and a square patch was connected to the ground through via holes.

Fig. 28 presents the results of $S_{6H,2H}$ and $S_{6H,3V}$ for the situation using PILI and EBG. In contrast to earlier results regarding the coupling between horizontal polarization, adjustable isolation notches were observed, and the isolation level has improved significantly. The isolation notches can be shifted by adjusting the EBG patch width. The results indicate that the resonant frequency decreased as the patch width increased, and advanced results can be obtained at the target frequency through optimization using this process. The results obtained in the presence of each isolator are presented in Fig. 28, where the electric filed is plotted. Fig. 29 (a), (b), and (c) display the field in the absence of an isolator, with PILI only, and with PILI and EBG, respectively. However, as the field intensity of the lower set's ports, they are still excited by the surface wave (i.e., there is the degradation of isolation even though PILI reduced the overall field distribution). This problem has been managed by using EBG, and the coupling of the lower set was completely removed, as implied by the electric field distribution shown in Fig. 29 (c).

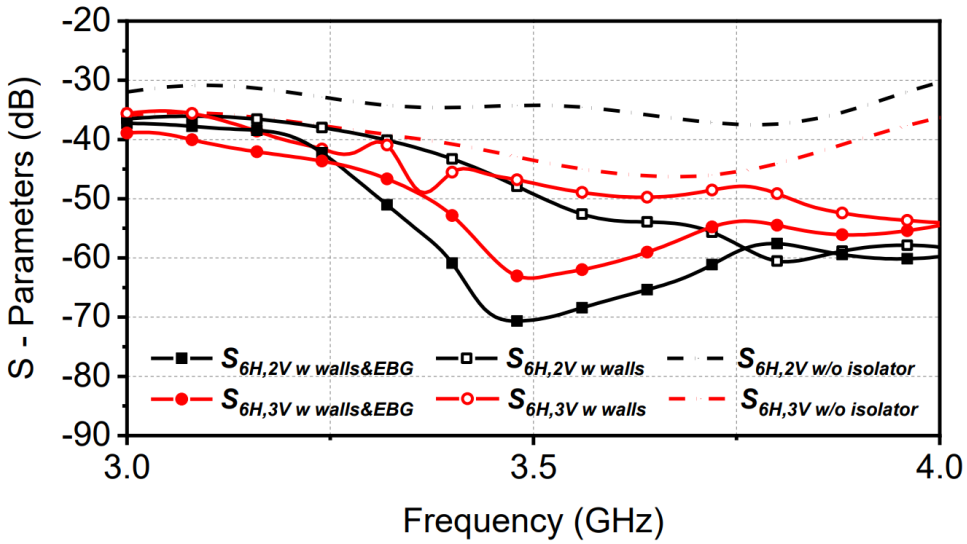

Figure 30. Electric field distribution of the array antenna system. (a) without the isolators, (b) with the PILI, and (c) with the PILI and EBG.

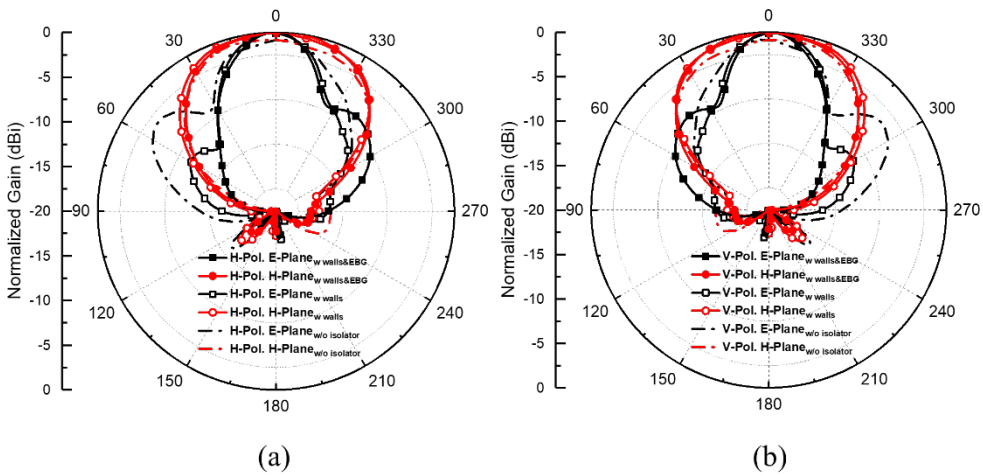

Figure 31. Beam patterns (***E***− and ***H***− planes) obtained in the simulation with respect to the presence of the isolator: (a) horizontal and (b) vertical polarizations.

As illustrated in Fig. 30, when there was no isolator, the isolation level had a value of approximately 40 dB for the vertical polarization, and when only the PILI was used, the isolation level improved by approximately 50 dB. However, the effect of the intended resonance structure was not observed. When PILI and EBG are used together, an

isolation notch can be made, and the isolation level improved to approximately 65 dB. Furthermore, Fig. 31 depicts the antenna beam patterns for the E- and H-planes. The half-power beamwidth (HPBW) was reduced by about 10°, and gain is enhanced by approximately 1 dB by introducing isolators because the PILI can be considered as PEC reflector (i.e., the reflected wave is combined as an in-phase). Although the HPBW decrease, the gain increased correspondingly. Thus, that channel capacity can be expected to improve based on Shannon's theorem.

3.3 Measurement and Analysis

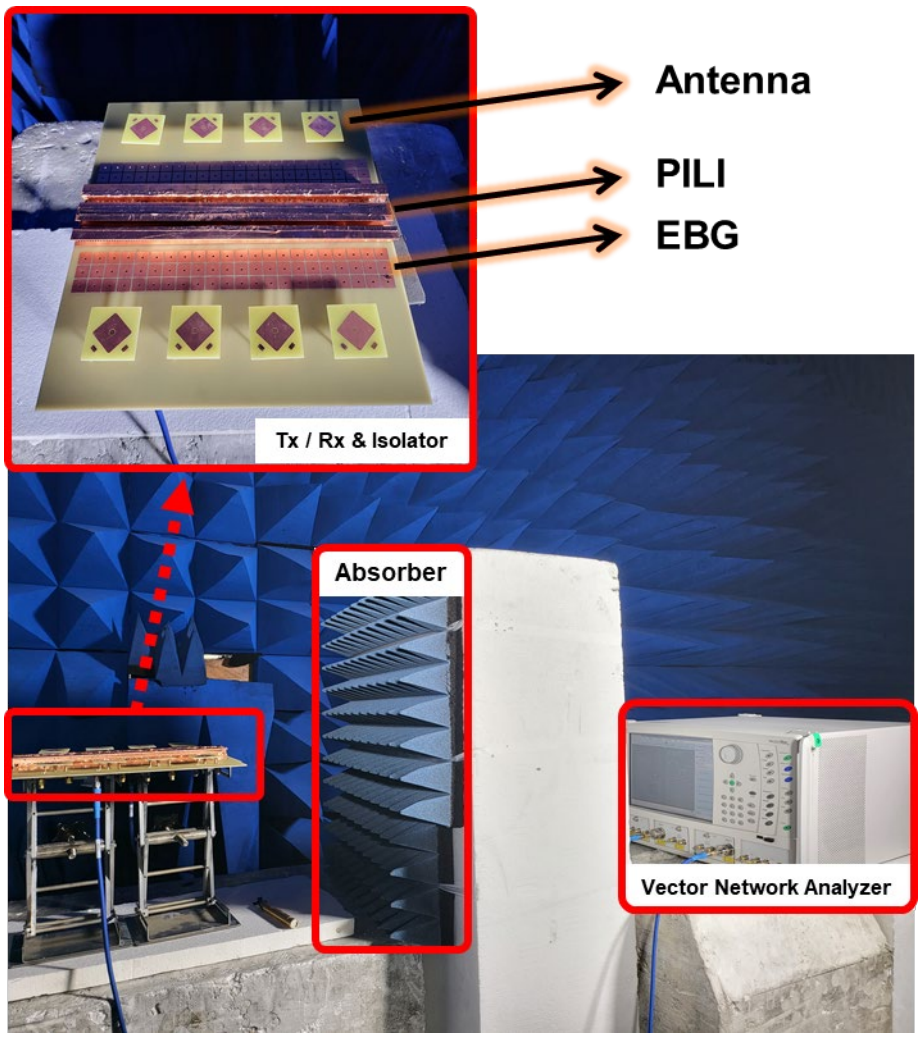

Figure 32. Fabricated antennas with the isolator composite and measurement setup.

The designed antenna and isolator were measured using an MS4747 vector network analyze in an anechoic chamber. As shown in Fig. 32, the other ports except for the two ports for measurement, were terminated; measurements were carried out. In addition, because the system had a very sensitive isolation level, an absorber was placed between the structure and the vector network analyzer due to the coupling caused by the reflection. To guarantee stable results for such as sensitive system, the calibration level was

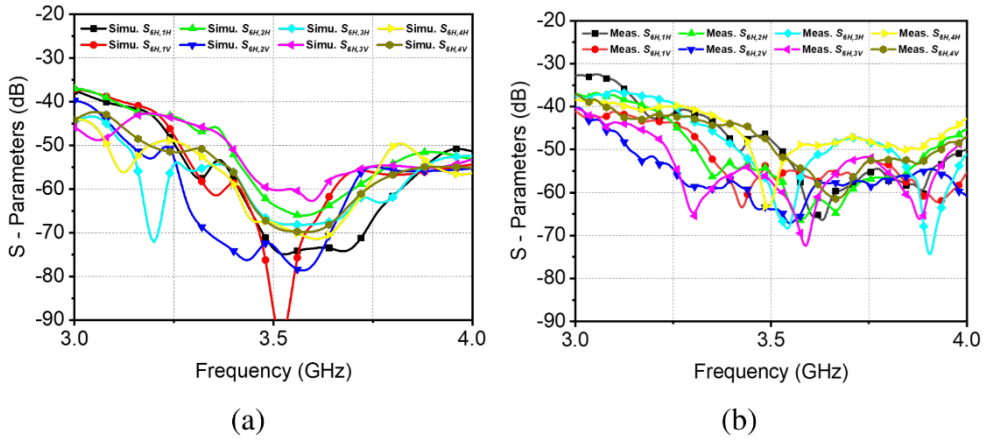

Figure 33. Results of the (a) simulation and (b) measurement of S-parameters for all array antennas.

maintained at about -60 dB during the measurement, and the reliability of the results was increased my maximizing the output power of the vector network analyzer.

Fig 33 (a) shows the results of the simulated coupling of the dual-polarization array antenna following the optimization. Eight results indicate the coupling of the four dual-polarized antennas of the upper set to the lower antennas. Thus, the isolation notches can be created at the target frequency if the previously suggested method uses two resonance structure of vertical and horizontal polarizations. Fig. 33 (b) indicates that isolation notches occurred at the target frequency for the measurement. However, unlike the simulation results, the notches were distributed with an error of 5% within a narrow band. This is because of a problem in the alignment, as the antenna and PILI are fabricated manually. It can be predicted that each antenna was rotated on an axis perpendicular to the plane of the substrate for the abovementioned reasons. In addition, because this problem occurs in the manufacture of the antenna and fabrication of PILI, the

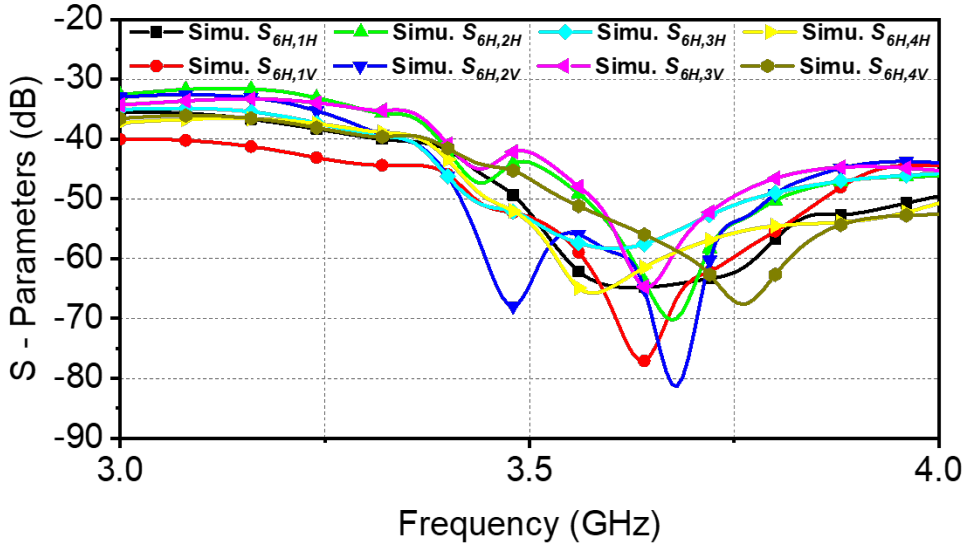

Figure 34. Results of simulation under practical conditions.

TABLE II
ISOLATOR PERFORMANCE COMPARISON TABLE

Ref.	Array Config.	Isolation Improvement	Pol.	Antenna Design	Profile
[28]	2 × 2	15 dB	dual	yes	0.4λ
[37]	4 × 2	20 dB	single	no	0.07λ
[38]	2 × 2	10 dB	dual	no	0.22λ
[39]	3 × 3	20 dB	dual	yes	0.51λ
This work	2 × 4	25 dB	dual	yes	0.14λ

corresponding environment is reflected in the simulation; the results are presented in Fig. 34. The simulation was conducted in a state where each antenna and PILI were rotated by ±5° with respect to the axis perpendicular to the plane of the substrate. Therefore, unlike the results illustrated in Fig. 33, which were obtained assuming ideal conditions, the isolation notches occurred with an error of 5% based on the target frequency. A comparison of the performance of the isolators used in various studied is presented in Table II. Although several researchers have found it challenging to improve the isolation for horizontal and vertical polarizations, this study effectively analyzed the coupling patch and obtained improved results for all polarizations and array antennas. Table II indicates that in addition to high isolation improvement, PILI has low-profile because of bent shape.

Chapter 4. Conclusion

For antenna, a novel concept and perspective for the design and analysis of dual-polarized antennas have been proposed in this study. First, a logical dual-polarized antenna was designed using the CM and DM theory, which has thus far been used for power divider design and improving the isolation of the array antenna. By making a slot in the radiator and connecting a metal stick, the electrical field distribution was efficiently changed, and consequently, superior isolation was achieved for the desired band. Further, the bandwidth ranged from 3.3 to 3.8 GHz, and up to 40 dB isolation was obtained. For the target band, the gain and total efficiency were obtained to be 8 dBi and 90%, respectively. Moreover, an active S-parameter and an additional beam pattern analysis were performed to consider the effect between the two ports when used simultaneously. It was proven that the proposed antenna works well for the target band. Both the simulated and experimentally measured results have proven that the proposed antenna is a great candidate for wireless communication systems with a simple configuration and low fabrication cost.

For isolator, a new concept was proposed the analysis of the metallic walls of planar inverted-L isolators for dual-polarized array antenna decoupling. The self-devised antenna is placed in an array and used in the decoupling system. Three possible paths were analyzed to address the coupling problem, and a structure to suppress coupling was presented for each path. PILI intuitively blocks the direct coupling. When they are directly connected to the ground, they can also suppress the ground coupling by adjusting the length of the walls to implement the resonance characteristics. Hence, horizontal

polarization has been improved for dual-polarized antennas; however, vertical polarization still requires improvement. The vertical polarization problem is thought to be caused by surface wave coupling, which is a coupling path that PILI cannot suppress. Therefore, an EBG that removes surface waves was used in conjunction with PILI. Consequently, the problem of vertical polarization was addressed, and each isolation level for the dual-polarized array antenna was as approximately 65 dB. Because the structure of the isolator and antenna are very complicated and there are too many EBG patches, designing an isolator with antennas is extremely difficult and laborious, requiring a very long simulation time and trial and error. In addition, the sensitivity of the system such as a very high isolation, sensitively alters the results. Therefore, it was difficult to manufacture an isolator using the PILI and EBG to achieve high isolation for each array and polarization. The proposed design overcomes a major limitation in the application of the dual-polarized array system to the IBFD's TRx operation and suggests a feasible way to build a high-performance system.

Bibliography

[1] K. E. Kolodziej, In-Band Full-Duplex Wireless Systems Handbook. Artech House, 2021.

[2] A. Sabharwal, P. Schniter, D. Guo, D. W. Bliss, S. Rangarajan, and R. Wichman, "In-band full-duplex wireless: Challenges and opportunities," *IEEE J. Sel. Areas Commun.,* vol. 32, no. 9, pp. 1637–1652, 2014.

[3] P. V. Prasannakumar, M. A. Elmansouri, and D. S. Filipovic, "Wideband decoupling techniques for dual-polarized bi-static simultaneous transmit and receive antenna subsystem," *IEEE Trans. Antennas Propag.*, vol. 65, no. 10, pp. 4991–5001, 2017

[4] J. Kim and J. Oh, "Liquid-crystal-embedded aperture-coupled microstrip antenna for 5g applications," *IEEE Antennas Wireless Propag. Lett.*, vol. 19, no. 11, pp. 1958-1962, 2020.

[5] R. Shanmugam, "Design and analysis of a frequency reconfigure-able penta-band antenna for wlan and 5g applications," *J. Electromagn. Eng. Sci.,* vol. 21, no. 3, pp. 228–235, 2021.

[6] Wong, K.-L. Lau, and K.-M. Luk, "Design of dual-polarized l-probe patch antenna arrays with high isolation," *IEEE Trans. Antennas Propag.,* vol. 52, no. 1, pp. 45–52, 2004.

[7] Q.-X. Chu, D.-L. Wen, and Y. Luo, "A broadband dual-polarized antenna with y-shaped feeding lines," *IEEE Trans. Antennas Propag.*, vol. 63, no. 2, pp. 483–490, 2015.

[8] S.-C. Gao, L.-W. Li, M.-S. Leong, and T.-S. Yeo, "Dual-polarized slot-coupled planar antenna with wide bandwidth," *IEEE Trans. Antennas Propag.*, vol. 51, no. 3, pp. 441–448, 2003.

[9] M. Ciydem and E. A. Miran, "Dual-polarization wideband sub-6 ghz suspended patch antenna for 5g base station," *IEEE Antennas*

Wireless Propag. Lett., vol. 19, no. 7, pp. 1142–1146, 2020.

[10] M. Li, X. Chen, A. Zhang, and A. A. Kishk, "Dual-polarized broadband base station antenna backed with dielectric cavity for 5g communications," *IEEE Antennas Wireless Propag. Lett.,* vol. 18, no. 10, pp. 2051– 2055, 2019.

[11] Q. Xue, S. W. Liao, and J. H. Xu, "A differentially-driven dual-polarized magneto-electric dipole antenna," *IEEE Trans. Antennas Propag.*, vol. 61, no. 1, pp. 425–430, 2012.

[12] L.-H. Wen, S. Gao, Q. Luo, Q. Yang, W. Hu, and Y. Yin, "A low-cost differentially driven dual-polarized patch antenna by using open-loop resonators," *IEEE Trans. Antennas Propag.,* vol. 67, no. 4, pp. 2745– 2750, 2019.

[13] D. M. Pozar, Microwave engineering. John wiley & sons, 2011.

[14] L. Sun, Y. Li, and Z. Zhang, "Decoupling between extremely closely spaced patch antennas by mode cancellation method," *IEEE Trans. Antennas Propag.,* vol. 69, no. 6, pp. 3074–3083, 2020.

[15] L. Sun, Y. Li, Z. Zhang, and H. Wang, "Antenna decoupling by common and differential modes cancellation," *IEEE Trans. Antennas Propag.*, vol. 69, no. 2, pp. 672–682, 2020.

[16] B. Qian, X. Chen, and A. A. Kishk, "Decoupling of microstrip antennas with defected ground structure using the common/differential mode theory," *IEEE Antennas Wireless Propag. Lett.*, vol. 20, no. 5, pp. 828– 832, 2021.

[17] L. Sun, Y. Li, and Z. Zhang, "Wideband decoupling of integrated slot antenna pairs for 5g smartphones," *IEEE Trans. Antennas Propag.*, vol. 69, no. 4, pp. 2386–2391, 2020.

[18] L. Sun, Y. Li, Z. Zhang, and H. Wang, "Self-decoupled mimo antenna pair with shared radiator for 5g smartphones," *IEEE Trans. Antennas Propag.*, vol. 68, no. 5, pp. 3423–3432, 2020.

[19] R. Hansen and M. Burke, “Antennas with magneto-dielectrics,” *Microw. Opt. Technol. Lett.*, vol. 26, no. 2, pp. 75–78, 2000.

[20] V. G. Kasabegoudar and K. Vinoy, “Coplanar capacitively coupled probe fed microstrip antennas for wideband applications,” *IEEE Trans. Antennas Propag.*, vol. 58, no. 10, pp. 3131–3138, 2010.

[21] C. X. Bai, Y. J. Cheng, Y. R. Ding, and J. F. Zhang, “A metamaterial-based s/x-band shared-aperture phased-array antenna with wide beam scanning coverage,” *IEEE Trans. Antennas Propag.,* vol. 68, no. 6, pp. 4283–4292, 2020.

[22] C. F. Ding, X. Y. Zhang, Y. Zhang, Y. M. Pan, and Q. Xue, “Compact broadband dual-polarized filtering dipole antenna with high selectivity for base-station applications,” *IEEE Trans. Antennas Propag.*, vol. 66, no. 11, pp. 5747–5756, 2018.

[23] W. L. Stutzman and G. A. Thiele, Antenna theory and design. John Wiley & Sons, 2012.

[24] . Liu, S. Wang, X. Wang, and Y. Jia, “A differentially fed dual-polarized slot antenna with high isolation and low profile for base station application,” *IEEE Antennas Wireless Propag. Lett.*, vol. 18, no. 2, pp. 303–307, 2018.

[25] S. J. Yang, Y. M. Pan, Y. Zhang, Y. Gao, and X. Y. Zhang, “Low-profile dual-polarized filtering magneto-electric dipole antenna for 5g applications,” *IEEE Trans. Antennas Propag.*, vol. 67, no. 10, pp. 6235–6243, 2019.

[26] D.-Z. Zheng and Q.-X. Chu, “A wideband dual-polarized antenna with two independently controllable resonant modes and its array for basestation applications,” *IEEE Antennas Wireless Propag. Lett.*, vol. 16, pp. 2014–2017, 2017.

[27] H. Huang, X. Li, and Y. Liu, “5g mimo antenna based on vector synthetic mechanism,” *IEEE Antennas Wireless Propag. Lett.*, vol. 17,

no. 6, pp. 1052–1055, 2018.

[28] C. Wei, Z.-Y. Zhang, and K.-L. Wu, “Phase compensation for decoupling of large-scale staggered dual-polarized dipole array antennas,” *IEEE Trans. Antennas Propag.*, vol. 68, no. 4, pp. 2822–2831, 2019.

[29] Y.-M. Zhang, J.-L. Li, S. Zhang, and G. F. Pedersen, “A transmission line-based decoupling method for mimo antenna arrays,” *IEEE Trans. Antennas Propag.,* vol. 67, no. 5, pp. 3117–3131, 2019.

[30] K. Wei, J.-Y. Li, L. Wang, Z.-J. Xing, and R. Xu, “Mutual coupling reduction by novel fractal defected ground structure bandgap filter,” *IEEE Trans. Antennas Propag.*, vol. 64, no. 10, pp. 4328–4335, 2016.

[31] Z. Wang, C. Li, and Y. Yin, “A meta-surface antenna array decoupling (maad) design to improve the isolation performance in a mimo system,” *IEEE Access*, vol. 8, pp. 61 797–61 805, 2020.

[32] S. Kim and S. Nam, “A compact and wideband linear array antenna with low mutual coupling,” *IEEE Trans. Antennas Propag.*, vol. 67, no. 8, pp. 5695–5699, 2019.

[33] Y.-M. Zhang and S. Zhang, “A side-loaded-metal decoupling method for 2× n patch antenna arrays,” *IEEE Antennas Wireless Propag. Lett.*, vol. 20, no. 5, pp. 668–672, 2021.

[34] M. Niroo-Jazi, T. A. Denidni, M. Chaharmir, and A. Sebak, “A hybrid isolator to reduce electromagnetic interactions between tx/rx antennas,” *IEEE Antennas Wireless Propag. Lett.*, vol. 13, pp. 75–78, 2013.

[35] K.-L. Wu, C. Wei, X. Mei, and Z.-Y. Zhang, “Array-antenna decoupling surface,” *IEEE Trans. Antennas Propag.*, vol. 65, no. 12, pp. 6728–6738, 2017.

[36] R. Abhari and G. V. Eleftheriades, “Metallo-dielectric electromagnetic bandgap structures for suppression and isolation of

the parallel-plate noise in high-speed circuits," *IEEE Trans. Microw. Theory Techn.*, vol. 51, no. 6, pp. 1629–1639, 2003.

[37] Y.-M. Zhang, S. Zhang, J.-L. Li, and G. F. Pedersen, "A wavetrap-based decoupling technique for 45◦ polarized mimo antenna arrays," *IEEE Trans. Antennas Propag.*, vol. 68, no. 3, pp. 2148–2157, 2019.

[38] S. Zhang, X. Chen, and G. F. Pedersen, "Mutual coupling suppression with decoupling ground for massive mimo antenna arrays," *IEEE Trans. Veh. Technol.,* vol. 68, no. 8, pp. 7273–7282, 2019.

[39] Y. Li and Q.-X. Chu, "Dual-layer superstrate structure for decoupling of dual-polarized antenna arrays," *IEEE Antennas Wireless Propag. Lett.*, vol. 21, no. 3, pp. 521–525, 2021.

초 록

본 논문은 안테나와 아이솔레이터로 구성된 송신기와 수신기의 전파영역 구현에 집중하였다. 첫 째로, 단순 파라미터 스터디가 아닌 새로운 관점의 논리적인 Common Mode and Differential Mode (CMDM)에 기반 설계 절차를 sub-6 GHz N78 밴드 (3.3-3.8 GHz)에 대하여 제시하였다. 다음으로, 이중편파 다중경로 커플링 억제를 위한 5G sub-6 GHz 대역 송수신기 안테나 어레이의 획기적인 구조와 디커플링 방법을 제시하였다.

안테나 설계에 대하여, S파라미터 모드 분할을 통한 필드 집중 방법을 이용하여 섬세한 설계법을 제시하였다. 흥미롭게도, 앞서 제시한 간단한 방법을 이용해서 각 모드에 독립적인 조절이 가능한 스미스 차트를 통해 각기 다른 편파 사이의 포트 격리도를 개선하였다. 이중편파 안테나의 동작원리에 대한 깊은 물리적 통찰력을 제공하기 위하여, CMDM 분석에 기반한 대응하는 필드 분포를 최초로 제시하였고 제안된 안테나는 시뮬레이션, 제작, 측정되었다. 시뮬레이션뿐만 아니라 실험을 통한 측정 결과는 안테나가 FR-4기판을 사용하여 저비용 제작을 하였고 40 dB의 포트 격리도, 8 dBi의 이득, 20 dB의 XPD, 92 %의 효율과 안정적인 빔패턴을 저자세로 얻었다. 게다가, 본 연구는 실제 동작 상황을 반영하기 위하여 Cross 편파에 대한 지식뿐만 아니라 active S파라미터를 가능한 모든 진폭과 위상조합에 대하여 제공했다.

아이솔레이터 설계에 대하여, 아이솔레이터 복합체는 평면 역-L 모양 (PILI)과 전자기파 밴드갭 (EBG)로 구성되어있다. 5G 실제 상황을 위하여 이중편파 다중격로를 고려하였다. 안테나는 40%의 임피던스 대역폭, 25 dB의 포트 격리도를 갖는다. 제안된 PILI는 송신기와 수신기 사이에 주요하게 직접적인 커플링과 그라운드를 통한 커플링을 억제할 수 있음이 증명되었다. EBG와 결합된 복합체는 추가로 이중편파 디커플링을 수행할 수 있다. 송신기 수신기를 반영하여, 1×4 어레이

안테나의 두 세트와 PILI/EBG 복합체가 8개의 결과를 동시에 만족하기 위하여 설계, 제작, 측정 되었다. 최종적으로, 측정된 결과는 임피던스와 포트 격리도는 유지하면서 전체적인 이중편파 어레이의 격리도는 대략 70 dB의 결과를 얻었다.

주요단어 : Fifth-generation (5G), 이중편파 안테나, 저비용, FR-4, common and differential mode, active s파라미터, XPD, 디커플링, 격리도, EBG, 송수신기 (TRx) 격리, 다중경로 격리, 상호 커플링
학 번 : 2021-25750